Pontifícia Universidade Católica
do Rio de Janeiro

Breno de Moura Calderoni

Levitated optomechanics: from Gaussian tweezers to structured modes

Dissertação de Mestrado

Dissertation presented to the Programa de Pós-Graduação em Física of PUC-Rio in partial fulfillment of the requirements for the degree of Mestre em Física.

Advisor: Prof. Thiago Barbosa dos Santos Guerreiro

Rio de Janeiro
October 2023

Pontifícia Universidade Católica
do Rio de Janeiro

Breno de Moura Calderoni

Levitated optomechanics: from Gaussian tweezers to structured modes

Dissertation presented to the Programa de Pós-Graduação em Física of PUC-Rio in partial fulfillment of the requirements for the degree of Mestre em Física. Approved by the Examination Committee:

Prof. Thiago Barbosa dos Santos Guerreiro
Advisor
Departamento de Física – PUC-Rio

Prof. Antonio Zelaquett Khoury
UFF

Prof. Tommaso Del Rosso
Departamento de Física – PUC-Rio

Rio de Janeiro, October the 23rd, 2023

Breno de Moura Calderoni

The author graduated in Applied Mathematics from Fundação Getulio Vargas do Rio de Janeiro in 2020.

Bibliographic data

de Moura Calderoni, Breno

Levitated optomechanics: from Gaussian tweezers to structured modes / Breno de Moura Calderoni; advisor: Thiago Barbosa dos Santos Guerreiro. – Rio de Janeiro: PUC-Rio, Departamento de Física, 2023.

v., 54 f: il. color. ; 30 cm

Dissertação (mestrado) - Pontifícia Universidade Católica do Rio de Janeiro, Departamento de Física.

Inclui bibliografia

1. Física – Teses. 2. Física – Teses. 3. Optomecânica;. 4. Pinça ótica;. 5. Potenciais não-lineares;. 6. Luz estruturada.. I. Barbosa dos Santos Guerreiro, Thiago. II. Pontifícia Universidade Católica do Rio de Janeiro. Departamento de Física. III. Título.

CDD: 530

Acknowledgments

Muitas pessoas que fizeram parte da minha vida no tempo em que estive na PUC e que merecem meu profundo e sincero agradecimento. Amizades novas, outras antigas que se fortaleceram, meus pais e o amor da minha vida.

Sem dúvida, minha trajetória não foi linear. De graduação em Matemática Aplicada na FGV, fui para o mestrado em Matemática na PUC. Insatisfeito, migrei para a Física sem saber ao certo com o que gostaria de trabalhar. No final, me encontrei na Física experimental. O Thiago Guerreiro me deu uma chance para trabalhar junto a seu grupo, foi meu maior professor e hoje o considero um amigo. Obrigado por ter me recebido, tentado me acalmar em momentos de ansiedade e por ter me ensinado tanto. Sem você eu provavelmente ainda estaria perdido na minha jornada.

Minha gratidão se estende a todos os membros do grupo. A verdade é que eu não poderia ter alcançado nada sozinho. Vocês me mostraram o melhor ambiente de trabalho possível e fiz verdadeiras amizades. Obrigado também pelas valiosas discussões.

Aos meus amigos de longa data, e futuros padrinhos do meu casamento, obrigado por sempre estarem presentes e me darem suporte emocional.

Se não fosse pelo apoio dos meus pais e o suporte que me deram por toda a vida seria inimaginável ter concluído o mestrado. Cresci num ambiente saudável onde minha educação sempre foi prioridade. Serei eternamente grato por isso.

Bruna, sem você é difícil imaginar onde estaria agora. A certeza que tenho é de que me sentiria menos completo e mais insatisfeito. Obrigado por estar sempre ao meu lado.

This study was financed in part by the Coordenação de Aperfeiçoaento de Pessoal de Nível Superior - Brasil (CAPES) - Finance Code 001.

Abstract

de Moura Calderoni, Breno; Barbosa dos Santos Guerreiro, Thiago (Advisor). **Levitated optomechanics: from Gaussian tweezers to structured modes**. Rio de Janeiro, 2023. 54p. Dissertação de Mestrado – Departamento de Física, Pontifícia Universidade Católica do Rio de Janeiro.

Optical tweezers have become an important tool in multidisciplinary research, allowing for the manipulation and study of micro- and nanoscale particles. Here, we describe the development of two optical tweezer experiments at the heart of levitated optomechanics: a Gaussian and a structured light vacuum optical tweezer. In the Gaussian experiment, we describe in detail its construction and its use to test features of stochastic motion subject to nonlinear effective forces generated via electric feedback. Next, we move to the structured light setup. Using a Spatial Light Modulator, we develop a vacuum optical tweezer with the capability of engineering arbitrary optical landscapes, including non-linearities and multi-particle traps. The experiments developed in this work pave the way to novel methods for controlling particle motion, forces and interactions, further extending the levitated optomechanics toolbox

Keywords

Optomechanics; Optical tweezer; Non-linear potentials; Structured light.

Resumo

de Moura Calderoni, Breno; Barbosa dos Santos Guerreiro, Thiago. **Optomecânica levitada: de pinças ópticas Gaussianas à modos estruturados**. Rio de Janeiro, 2023. 54p. Dissertação de Mestrado – Departamento de Física, Pontifícia Universidade Católica do Rio de Janeiro.

As pinças ópticas tornaram-se uma ferramenta importante na pesquisa multidisciplinar, permitindo a manipulação e estudo de partículas em micro e nanoescala. Aqui, descrevemos o desenvolvimento de dois experimentos de pinça óptica no cerne da optomecânica levitada: uma pinça óptica a vácuo Gaussiana e uma pinça óptica a vácuo com luz estruturada. No experimento Gaussiano, descrevemos em detalhes sua construção e seu uso para testar características de movimento estocástico sujeito a forças efetivas não-lineares geradas através de feedback elétrico. Em seguida, passamos para a configuração de luz estruturada. Utilizando um Modulador Espacial de Luz, desenvolvemos uma pinça óptica a vácuo com a capacidade de gerar potenciais ópticos arbitrários, incluindo não-linearidades e armadilhas para múltiplas partículas. Os experimentos desenvolvidos neste trabalho abrem caminho para novos métodos de controle de movimento de partículas, forças e interações, expandindo ainda mais a caixa de ferramentas da optomecânica levitada.

Palavras-chave

Optomecânica; Pinça ótica; Potenciais não-lineares; Luz estruturada.

Table of contents

List of figures

1
Introduction

The interaction of light with matter has been a pivotal subject in scientific discourse [1], significantly shaping our understanding of physics. It has long been established that light carries momentum [2,3], but the tangible exploration of this phenomenon became more feasible with the advent of laser technology in the 1960s [4]. This technological advance facilitated extensive studies on radiation pressure and enabled scientists to observe the subtle forces exerted by light on macroscopic objects [2, 5].

Arthur Ashkin pioneered the exploration of optical tweezers, illustrating that focused laser beams could trap and confine dielectric micrometer particles [6, 7]. This development of optical tweezers stemmed from the coherent nature of laser light, allowing for the accurate manipulation and study of particles ranging from the nano to the micro scale [8].

Levitodynamics [9], involving the trapping and controlling of nano- and micro-objects in a vacuum [10, 11], emerged as a novel field, blending principles from atomic physics [12, 13], biophysics [14], and other domains [15, 16]. It has allowed scientists to analyse the dynamics of levitated objects in high vacuum, offering insights into non-equilibrium physics [17, 18], thermodynamics [19–22], and various material properties under distinct conditions [23, 24].

Optical tweezers have found extensive applications across diverse scientific fields, notably in biology for analyzing physical properties of cell membranes [25], and in physics as force sensors [26–28]. The ability to manipulate and study the motion and properties of particles and atoms in isolation has been instrumental in deepening our understanding of quantum mechanics and the interactions between light and matter [29–32].

My dissertation aims to add to this growing field by focusing on two experiments designed to expand our current understanding. The first one experimentally validates predictions made by perturbation theory [33] regarding the introduction of an effective quartic harmonicity on a nanoparticle suspended in an optical trap. The work compares configurations to both theoretical expectations and numerical simulations [34]. A second experiment is introduced that addresses the inherent limitations of conventional optical trapping techniques in manipulating particles within complex potential landscapes [35,36].

This segment explores the utilization of structured light in vacuum optical tweezers, employing a Spatial Light Modulator to create an optical bottle beam [37, 38], forming a double potential well along the beam's propagation direction. This enables the simultaneous trapping of two particles on the beam's propagation direction, opening avenues for advanced experiments and applications involving controlled inter-particle interactions [39].

The structure of this dissertation is designed for a logical progression of thought, segmented into four more chapters. The second chapter, "Theory of Vacuum Optical Tweezers", delves into the theory of the subject, providing the scientific context and theoretical basis upon which the experiments were conceived and executed. In the third chapter, "Experimental Tweezer in Vacuum", we elucidate the setup, data collection, and findings of the first experiment. The fourth chapter, "Structured Light Vacuum Optical Tweezer", serves as an exploratory segment discussing the innovative techniques and preliminary results of the second experiment. The fifth and final chapter offers a conclusion and outlook, summarizing the findings and offering perspectives on potential future work.

2
Theory of Vacuum Optical Tweezers

To comprehend the underlying physics of optical trapping, it is first necessary to understand about the spatial profile of laser beams and the motion dynamics of the object in the trap. We start this chapter with a theoretical introduction on the paraxial Helmholtz equation and their solutions: the Gaussian, Hermite Gaussian and Laguerre Gaussian beams, commonly employed in optical trapping. Next, we briefly describe the stochastic motion of a trapped particle and its spectral analysis, necessary for the trap characterization.

2.1
Optical Tweezers

In 1970, the 2018 Nobel Laureate Arthur Ashkin demonstrated that with the force of radiation pressure of a continuous laser it is possible to manipulate microscopic particles [5, 40]. This manipulation is made possible because light is made up of oscillating electric and magnetic fields that propagate through space. As these fields move, they carry energy and momentum. When photons, or light particles, strike the particle's surface, they transfer momentum to it. This transfer of momentum from the photons to the particle generates a force [7]. These optical forces can be thought of as produced by the intensity and gradient intensity of the laser beam. To better understand optical trapping, we must therefore first introduce the spacial profiles of laser beams.

2.1.1
Paraxial Helmholtz Equation and its Solutions

Maxwell's equations describe the dynamics of electric and magnetic fields in space-time. A consequence of the Maxwell's laws of electrodynamics is the wave equation for an electric field $\vec{E}(\vec{r}, t)$. For a certain class of solutions in vacuum[1] (that is, in the absence of charges and currents) which we refer to as scalar light fields, we may write the electric field as $\vec{E}(\vec{r}, t) = U(\vec{r}, t)\hat{\epsilon}$, where $U(\vec{r})$ is a mode function describing the spacial-temporal profile of the electric field and $\hat{\epsilon}$ is the field's polarization vector. Throughout this thesis, we will assume the polarization vector to be constant. Therefore, the wave equation

[1]We will not deal here with vector light fields, see [41] for a comprehensive review.

may be written as

$$\nabla^2 U = -\frac{1}{c^2}\frac{\partial^2 U}{\partial t^2} \ . \tag{2-1}$$

Substituting $U(\vec{r},t) = U(\vec{r})\exp(i\omega t)$ into Eq. (2-1), we arrive at the *Helmholtz equation*,

$$\nabla^2 U + k^2 U = 0, \tag{2-2}$$

where ω represents the angular frequency and k is the wavenumber, which are related by $c = \omega/k$.

For laser beams that are not tightly focused the *small angle*, or paraxial approximation, can be applied. We write the spacial mode function as

$$U(\vec{r}) = E(\vec{r})e^{ikz} \tag{2-3}$$

The paraxial approximation then reads

$$\left|\frac{\partial^2 E}{\partial z^2}\right| \ll \left|k\frac{\partial E}{\partial z}\right| \tag{2-4}$$

which physically means that the mode envelope $E(\vec{r})$ varies slowly in the longitudinal direction. When combined with the Helmholtz equation, this leads to the paraxial Helmholtz equation,

$$\nabla_T^2 E - 2ik\frac{\partial E}{\partial z} = 0. \tag{2-5}$$

where ∇_T^2 denotes the Laplacian operator in the transverse coordinates. Beams satisfying this equation are called paraxial beams. Altought the paraxial wave equation is not ideal to describe tightly focused fields, as in the optical tweezers studied in this work, the mode structure of paraxial beams is still a good description for most situations and effective corrections to the beams' parameters can be employed to account for the effects of tight focusing [42]; we will turn to this issue later on, when we discuss the optical trapping experiment results.

The complete set of solutions for the paraxial Helmholtz equation is constituted by either the Hermite-Gaussian beams (HG) in Cartesian coordinates or, in cylindrical coordinates, the Laguerre-Gaussian beams (LG). This implies that any two-dimensional light field can be represented as a superposition of these modes, which leads to new opportunities and applications for vacuum optical traps - a topic that will be explored in Chapter 4.

Hermite-Gaussian beams take the form,

$$\begin{aligned} E_{m,n}^{HG}(x,y,z) =& E^G(x,y,z)H_m\left(\sqrt{2}\frac{x}{W(z)}\right) \\ &\times H_n\left(\sqrt{2}\frac{y}{W(z)}\right)\exp\left[-i(m+n)\zeta(z)\right], \end{aligned} \tag{2-6}$$

$$H_m(x) = \exp\left(x^2/2\right)\left(x - \frac{d}{dx}\right)^m \exp\left(x^{-2}/2\right), \tag{2-7}$$

where H_n are the Hermite polynomials. The optical intensity of HG modes reads,

$$I^{HG}_{m,n}(x,y,z) = I_0 \left(\frac{W_0}{W(z)}\right)^2 \exp\left[-\frac{x^2+y^2}{W^2(z)}\right] H_m\left(\sqrt{2}\frac{x}{W(z)}\right)^2 \times H_n\left(\sqrt{2}\frac{y}{W(z)}\right)^2. \tag{2-8}$$

where E_0 the mode amplitude and W_0 is the beam waist, which assume to be located at the origin of our coordinate system, at the focal point $(x, y, z) = (0, 0, 0)$.

We may say that what characterizes the HG modes is their Cartesian symmetry. The indices m and n dictate the beam profile shape along the x and y axes, respectively. Specifically, with m nodes in the x-direction and n nodes in the y-direction. Fig-2.1 illustrates the HG beam for different values of m and n.

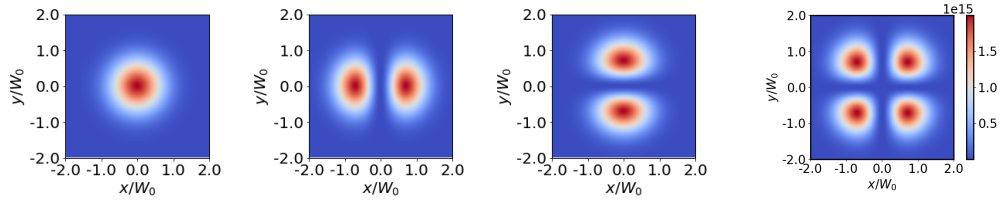

(a) $HG_{0,0}$ (b) $HG_{1,0}$ (c) $HG_{0,1}$ (d) $HG_{1,1}$

Figure 2.1: Hermite Gaussian beams in the transverse plane for different mode parameters m and n

The Laguerre-Gauss solutions are

$$E^{LG}_{p,l}(\rho,\phi,z) = E^G(\rho,z)\left(\sqrt{2}\frac{\rho}{W(z)}\right)^l L^l_p\left(2\frac{\rho^2}{W(z)^2}\right) \times \exp\left[-i(2p+l)\zeta(z) + il\phi\right] \tag{2-9}$$

$$L^l_p = \frac{x^{-l}}{p!}\left(\frac{d}{dx} - 1\right)^p x^{p+l} \tag{2-10}$$

where L^l_p are the Laguerre polynomials. Their optical intensity is,

$$I_{p,l}^{LG}(\rho,\phi,z) = I_0 \left(\frac{W_0}{W(z)}\right)^2 \exp\left[-\frac{\rho^2}{W^2(z)}\right] \left(-\frac{2\rho^2}{W(z)^2}\right)^l \times \left(L_p^l \frac{2\rho^2}{W(z)^2}\right)^2 \tag{2-11}$$

where the transverse radial coordinate reads $\rho = \sqrt{x^2 + y^2}$.

The LG beams have cylindrical symmetry. The parameters p and l specify the number of radial nodes and the azimuthal phase distribution, respectively. Like HG beams, LG beams also form a complete orthogonal basis of solutions for the paraxial wave equation.

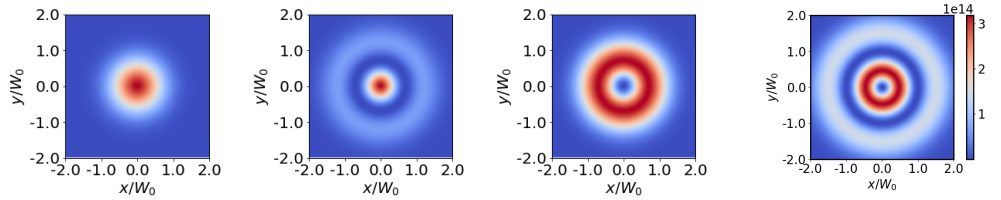

(a) $LG_{0,0}$ (b) $LG_{1,0}$ (c) $LG_{0,1}$ (d) $LG_{1,1}$

Figure 2.2: Laguerre Gaussian beams in the transverse plane for different mode numbers p and l

The fundamental solution of the paraxial wave equation, and the most commonly employed laser profile is known as the Gaussian beam, represented both by $LG_{0,0}$ and $HG_{0,0}$. It earns its name due to its intensity distribution, given by the Gaussian function.

The expression for the Gaussian beam reads

$$E^G(\rho,z) = E_0 \frac{W_0}{W(z)} \exp\left[-\frac{\rho^2}{W(z)^2} + ik_m z - i\zeta(z) + ik_m \frac{\rho^2}{2R(z)}\right]. \tag{2-12}$$

where we introduce the following important beam parameters,

$$W(z) = W_0\sqrt{1 + \frac{z^2}{z_R^2}}, \qquad \text{Beam width} \tag{2-13}$$

$$R(z) = z\left(1 + \frac{z_R^2}{z^2}\right), \qquad \text{Wavefront radius} \tag{2-14}$$

$$\zeta(z) = \arctan\left(\frac{z}{z_R}\right), \qquad \text{Gouy phase} \tag{2-15}$$

$$z_R = \frac{\pi W_0^2}{n_m \lambda_0}, \qquad \text{Rayleigh range} \tag{2-16}$$

The Gouy phase, or phase correction, describes how the beam's phase varies from a plane wave while it propagates. The Rayleigh range represents the

distance from the beam waist where the beam radius is increased by a factor of $\sqrt{2}$, i.e. the area is doubled. This distance also dictates the region over which the beam is approximately non-expanding, or collimated, give by $2z_R$, also known as the depth-of-focus. Here, n_m is the refractive index of the medium where the beam is propagating.

Given the Gaussian bema waist W_0 we an define another important definition: the numerical aperture (NA). It can be expressed as

$$\mathrm{NA} = n_m \sin\theta = \frac{n_m \lambda_0}{\pi W_0}, \tag{2-17}$$

with θ being the half-angle of divergence of the beam. Using (2-16) and (2-17)we may also write z_R in terms of the NA as,

$$z_R = \frac{n_m \lambda_0}{\pi \mathrm{NA}^2}, \tag{2-18}$$

Fig-2.3 shows all the relevant parameters of a Gaussian beam in a succinct manner.

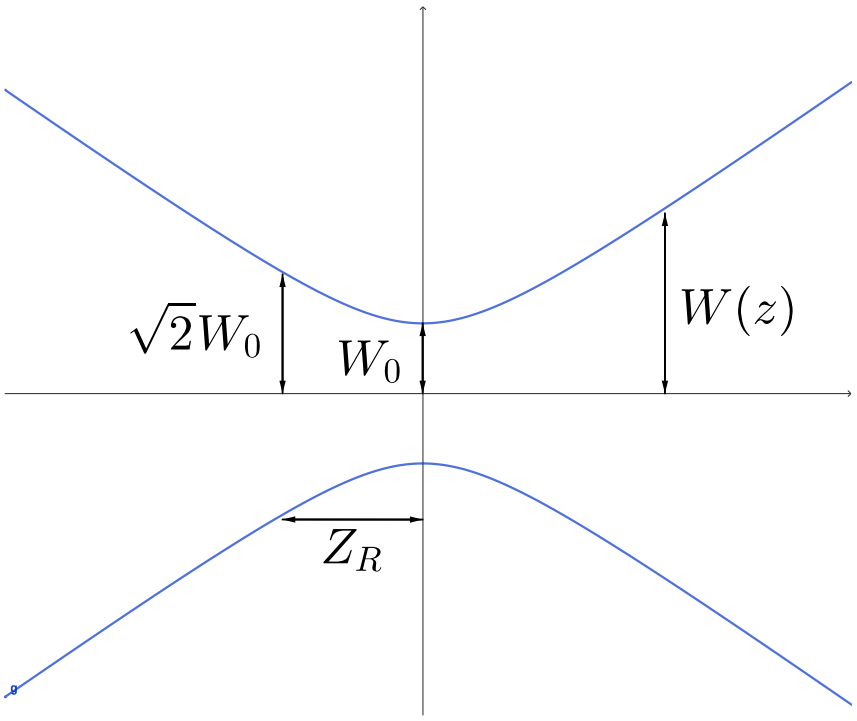

Figure 2.3: Representation of the beam waist, beam width and Rayleigh range of a Gaussian beam.

The optical intensity of the Gaussian mode,

$$I^G(\rho, z) = I_0 \left(\frac{W_0}{W(z)}\right)^2 \exp\left[-\frac{2\rho^2}{W^2(z)}\right] \tag{2-19}$$

where $I_0 = |E_0|^2$. On the beam axis $\rho = 0$ the Gaussian function peaks and we can then write,

$$I(0,z) = I_0 \left(\frac{W_0}{W(z)} \right)^2 = \frac{I_0}{1 + \left(\frac{z}{z_R} \right)^2} \tag{2-20}$$

from which we define the location of the greatest intensity at the center, $I(0,0) = I_0$. The bell shaped graph can be seen in Fig-2.4.

Figure 2.4: Normalized beam intensity at $\rho = 0$

.

To calculate the total optical power, one has to integrate the optical intensity over the whole transverse plane,

$$P = \int_0^\infty I(\rho, z) 2\pi\rho d\rho. \tag{2-21}$$

Upon solving the integration, we obtain the total optical power,

$$P = \frac{1}{2} I_0 \pi W_0^2. \tag{2-22}$$

With this result, the intensity can also be expressed in terms of P as

$$I(\rho, z) = \frac{2P}{\pi W^2(z)} \exp\left[-\frac{2\rho^2}{W^2(z)} \right]. \tag{2-23}$$

In the following chapter, we will employ a Gaussian mode as the trapping beam in our optical tweezer experiments. Later on, we will modify our optical trap to produce higher order modes for optical trapping. Having defined the intensity of the Gaussian beam, we are now in a position to discuss the forces that act on a particle in standard optical tweezers.

2.2 Optical Force in the Dipole Regime

Back in the 70's[2], Arthur Ashkin identified two fundamental light forces exerted on a dielectric particle in a laser field. These are the scattering force $\vec{F}_{scat}(\vec{r})$ – in the propagation direction of the incident beam – and a gradient force $\vec{F}_{grad}(\vec{r})$, along the intensity gradient of the beam. Ashkin conducted experiments [5–7, 10, 25, 40] and showed that this forces could accelerate, decelerate and trap the particle in a stable optical potential well. Finally, in 1986, he observed the first optical tweezer in a experiment using a tightly focused laser beams.

The gradient force is a conservative force that is originated from the potential energy of a dipole within an electric field. The scattering force, on the other hand, is a non-conservative force arising from the momentum transfer from

[2]It is interesting to compare the date of invention of the laser to the invention of the optical tweezer!

the field to the particle, which is a consequence of scattering and absorption processes.

Optical forces acting on spherical particles can be categorized into three regimes: the Rayleigh regime, the intermediate regime and the ray optics regime, based on the particle size and wavelength of the beam. The size parameter ξ can be defined as $\xi = k_m R$, where $k_m = 2\pi n_m/\lambda_0$, R is the radius of the particle, n_m the refractive index of the medium and λ_0 the wavelength of the trapping beam in a vacuum. When $\xi \gg 1$ (commonly assumed to be $R > 10\lambda_0$), the force can be described by the ray optics regime. In contrast, the Rayleigh regime is when $\xi \ll 1$ (commonly assumed to be $10R < \lambda_0$) and the particle can be approximated as a dipole in a laser field. For particles with sizes between these two regimes, the Lorenz-Mie theory can be utilized to investigate the optical force in the intermediate regime. Calculations in the intermediate regime are complicated, and numerical methods have to be employed for predicting the properties of optical forces. For example, the numerical toolbox developed in [43] can be used to estimate trap characteristics in the Lorentz-Mie regime.

In this dissertation we will focus primarily on the dipole regime, since our particles have a radius of $R = 72\,\text{nm}$ and the wavelength of the trapping laser is $\lambda = 780\,\text{nm}$. In this regime, the optical gradient and scattering forces can be calculated analytically using Rayleigh scattering theory [44]. The forces are [45],

$$\vec{F}_{grad}(\vec{r}) = \frac{2\pi n_m R^3}{c}\left(\frac{m^2-1}{m^2+2}\right)\nabla I(\vec{r}) \tag{2-24}$$

$$\vec{F}_{scat}(\vec{r}) = \frac{128\pi^5 n_m^5 R^6}{3c\lambda_0^4}\left(\frac{m^2-1}{m^2+2}\right)^2 I(\vec{r})\hat{z} \tag{2-25}$$

where c is the speed of light in vacuum and $m = n_p/n_m$ is the so-called refractive index ratio, with n_p the refractive index of the particle and $\hat{z}$ the unit vector along the beam propagation direction z. When the refractive index of the particle n_p is greater than that of its surrounding medium n_m, the gradient force pushes the particle towards the region of highest intensity. On the other hand, when n_p is smaller than n_m, the gradient force pushes the particle away. For standard optical trapping in vacuum, we want the first condition. The total force on the particle can be approximated as $\vec{F}(\vec{r}) = \vec{F}_{\text{grad}}(\vec{r}) + \vec{F}_{\text{scat}}(\vec{r})$. A plot of the gradient and scattering forces along the longitudinal (z) direction for the relevant parameters in our experiments can be seen in Fig-2.5.

In addition to the gradient and scattering, there is a third force referred to as *spin-curl* force [45, 46]. It arises due to polarization gradients within the

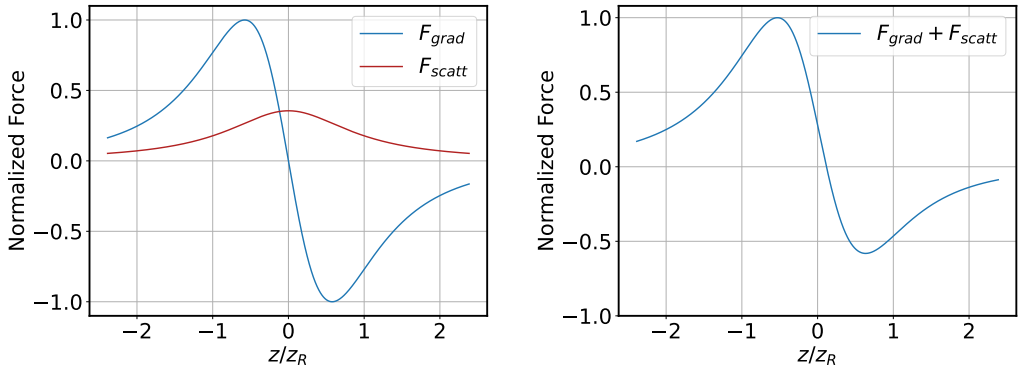

Figure 2.5: Forces applied on the trapped particle along the z-axis. On the left, the F_{grad} and F_{scatt} discriminated. On the right, the total resulting force. Parameters used for the plot are $\lambda_0 = 780\,\text{nm}$, NA $= 0.77, P = 200\,\text{mW}, n_m = 1.0, n_p = 1.45$ and $R = 72\,\text{nm}$, similar to those employed in our experimental setup.

electromagnetic field, but since we are considering beams with homogeneous polarization, these forces are negligible in our setup.

The gradient force is particularly important as it establishes a confining potential for the particle. This potential is a measure of the energy required to move the particle within the trap and can be described mathematically by,

$$V(\vec{r}) = -\frac{2\pi n_m R^3}{c}\left(\frac{m^2-1}{m^2+2}\right) I(\vec{r}). \tag{2-26}$$

For successful trapping of the particle, the gradient force must exceed the scattering force, or otherwise the particle will be pushed along the direction of beam propagation. The well depth of the trapping potential, defined through Eq (2-26), serves as a critical figure of merit for stable trapping. According to the Maxwell-Boltzmann distribution of the particle's kinetic energy at thermal equilibrium [47], the well depth should be at least one order of magnitude greater than the particle's average kinetic energy [48]. The average kinetic energy in thermal equilibrium can be calculated as $3k_BT/2$, based on the energy equipartition theorem [47], where k_B is the Boltzmann constant, and T is the temperature of the medium. Notably, although the average kinetic energy remains constant irrespective of the particle size, the well depth diminishes as the particle size decreases, making it more challenging to trap smaller particles.

This leads us to consider the size-dependence of the forces and the trapping potential. Specifically, the gradient force scales as R^3, contrasting with the scattering force which scales as R^6. This distinction in scaling elucidates the presence of an upper limit for the particle radius, R, where the gradient force can dominate the scattering force, assuming all other variables remain constant. To further examine the lower limit for R we must ensure that the minimum

potential well depth, $V_{\min}$, substantially exceeds the particle's kinetic energy, satisfying the conditions $V_{\min} \gg 3k_BT/2$ or we may adopt $V_{\min} > 15k_BT$.

Another important feature of the optical force provided by a Gaussian laser beam is that it can be approximated by a linear function of the particle's position near the origin (the beam waist). This can already be noticed in the linear behavior of the force near the origin, in Fig-2.6. In other words, the force from a Gaussian beam is approximately harmonic [49]. More specifically, we can write

$$\vec{F} = -k_x x\hat{x} - k_y y\hat{y} - k_z z\hat{z} \tag{2-27}$$

where $k_{x,y,z}$ denotes the spring constants along the x, y and z directions. To find the values of the spring constants in terms of the trapping beam's parameters, we need to expand the intensity $I(\rho, z)$ (as given in Eq. (2-23)) in a Taylor series around the equilibrium point ($z = 0$). We have,

$$I(\rho, z) \approx \frac{2Pn_m}{\pi W_0^2} - \frac{2Pn_m}{\pi W_0^2 z_R^2} z^2 - \frac{4Pn_m}{\pi W_0^4}\rho^2 \tag{2-28}$$

Since the intensity is proportional to the potential energy, we can directly use the above equation to determine the spring constants. For the z-direction,

$$\begin{aligned} k_z &= \frac{2\pi n_m R^3}{c}\left(\frac{m^2-1}{m^2+2}\right)\frac{4Pn_m}{\pi W_0^2 z_R^2} \\ &= \frac{8\pi^4 R^3 P \mathrm{NA}^6}{c n_m^2 \lambda_0^4}\left(\frac{m^2-1}{m^2+2}\right) \end{aligned} \tag{2-29}$$

The calculation for the x and y directions is analogous. We find,

$$k_x = k_y = \frac{16\pi^4 R^3 P \mathrm{NA}^4}{c n_m^2 \lambda_0^4}\left(\frac{m^2-1}{m^2+2}\right) \tag{2-30}$$

Typically, the order-of-magnitude of the spring constant is of $0.1 \sim 10\,\mathrm{pN}/\mu\mathrm{m}$. In the paraxial approximation we find that the spring constants along the x and y directions are equal. In reality, for a tightly focused beam, this is not the case [42], as we will later see in the experiment.
Notice also the trapping force is stronger in the x and y directions, compared to the z direction. That leads to the central frequency motion of the particle on z direction to be smaller that on x and y directions.

In a circularly polarized Gaussian beam with a perfectly aligned setup, k_x and k_y should be identical [45]. However, in real-world applications, factors such as slight misalignments, imperfections in the optical components, aberrations and the effects of tight focusing mentioned above can lead to differences between k_x and k_y.

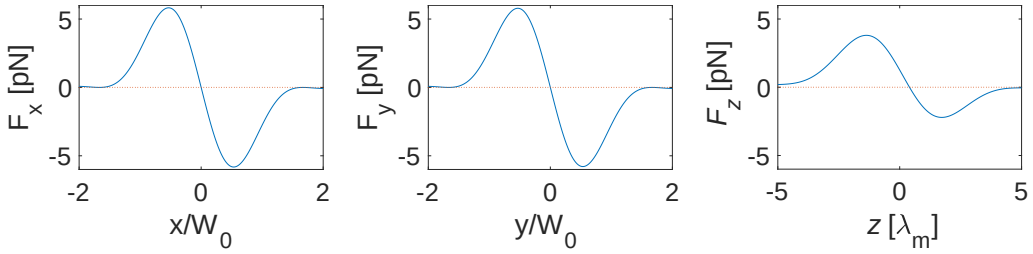

(a) Force on x-direction (b) Force on y-direction (c) Force on z-direction

Figure 2.6: Optical forces on an optically trapped nanoparticle. Parameters used for the plot are $\lambda_0 = 780\,\text{nm}$, NA $= 0.77$, $P = 200\,\text{mW}$, $n_m = 1.0$, $n_p = 1.45$ and $R = 72\,\text{nm}$

The analysis of forces on a trapped particle naturally leads us to study its stochastic motion within the trap. The interplay between gradient and scattering forces and the random Brownian motion caused by interaction of the particle with its surrounding medium, dictates the overall dynamics and behavior of the particle within the optical trap. Understanding this dynamics is pivotal as it provides a comprehensive view of the trapped particle's actions and reactions and the trap characteristics.

2.3 Stochastic motion

Stochastic motion, characterized by the random movement of a particle, arises primarily due to influences of the surrounding medium. This behavior of particles suspended in a fluid, typically resulting from their collision with the fast-moving molecules of the fluid, is mathematically modeled by the Langevin equation. This equation is crucial in the analysis of different types of stochastic processes, as it combines deterministic forces with stochastic forces, becoming a straightforward way to introduce noise into a system [45].

2.3.1 Langevin equation

By incorporating a fluctuating force into Newton's equation of motion for a particle with mass m, one obtains the Langevin equation,

$$m\frac{d^2}{dt^2}\vec{r}(t) = -\gamma\frac{d}{dt}\vec{r}(t) - \nabla V(\vec{r}) + \sqrt{2\gamma k_B T}\vec{\eta}(t), \tag{2-31}$$

where $\vec{r}(t)$ is the trapped particle's stochastic trajectory and γ is the damping coefficient, which can be determined by Stoke's law,

$$\gamma = 6\pi\rho\nu R \tag{2-32}$$

in a fluid with shear viscosity $\rho\nu$, ρ the fluid's density, ν its kinematic viscosity. The last term contains the random force $\vec{\eta}(t)$, which has zero mean and whose components satisfy,

$$\langle \eta_i(t)\eta_j(t')\rangle = \delta_{ij}\delta(t-t') \tag{2-33}$$

From the Langevin equations we can compute the particle's position correlation functions and the associated power spectral densities (PSDs), which contain important information on the trap characteristics. We will not re-derive the PSDs from the Langevin equation here, as that has been done in a number of texbooks [45]. In the next section, we introduce the necessary concepts and results used in the remaining of this work.

Another important concept is the Reynolds number of a particle, which aims to characterize whether the particle is in an underdamped or overdamped system. It is given by the ratio between the magnitudes of inertial and viscous forces acting on an object moving through a fluid by

$$Re = Rv\rho/\nu, \tag{2-34}$$

where v is the terminal velocity. An underdamped system has a high Reynolds number (commonly assumed to be $Re > 100$), where the inertia of the particle $m\frac{d^2}{dt^2}r(t)$ is not negligible compared to the damping term $\gamma\frac{d}{dt}r(t)$. This leads to oscillatory behavior where the particle can overshoot its equilibrium position. On the other hand, the overdamped system is when the viscosity, or damping term, dominates over inertia (commonly used as $Re < 100$). Since we will deal with optical tweezers in vacuum, we will be mostly concerned with high Reynolds numbers [45].

2.3.2 Power Spectral Analysis

One of the primary methods used for calibrating optical tweezers is measuring the particle position's power spectral density (PSD) [45].

Focusing on the longitudinal direction, the PSD of the $z(t)$ coordinate is the squared modulus of its auto-correlation Fourier transform [50],

$$P(\omega) = \int_{-\infty}^{\infty} \langle z(\omega)z(\omega')\rangle d\omega' \tag{2-35}$$

One can also show that

$$P(\omega) = |\tilde{z}(\omega)|^2 \tag{2-36}$$

where,

$$\tilde{z}(\omega) = \int_{-\frac{T_{rec}}{2}}^{\frac{T_{rec}}{2}} z(t)e^{i\omega_k t}dt \tag{2-37}$$

with T_{rec} the time duration of the recorded positions of a trapped nanoparticle.

Starting from the Langevin equation (2-31) with a harmonic potential, the PSD of the particle motion on the underdamped regime assumes the Lorentzian form [45],

$$P(f) = \frac{D/2\pi^2}{(f_c - 2\pi m/\gamma f^2)^2 + f^2}, \tag{2-38}$$

where $D = k_B T/\gamma$ is the diffusion coefficient, $f_c = k/2\pi\gamma$ is the corner frequency and k the trap stiffness. Notice that (2-38) is a type of Lorenztian function because it can be written in the standard form,

$$P(f) = \frac{A}{(f - f_0)^2 + \Gamma^2} \tag{2-39}$$

where A, f_0 and Γ are constants. Let $A = D/2\pi^2$, $f_0 = f_c$ and $\Gamma = 2\pi m/\gamma f^2$.

The peak is acquired at the trap's natural frequency $f_m = (2\pi)^{-1}\sqrt{k/m}$ and the width of the peak will be determined by the damping coefficient γ.

This entire set of information will be utilized in subsequent chapters to characterize the stochastic motion of optically trapped nanoparticles in experiments.

3
Experimental Tweezer in Vacuum

In this chapter, we focus on the experimental aspects of optical tweezers operating in vacuum. We describe the construction of the setup and trap characterization, employing the concepts described in the previous chapter. Finally, we discuss the application of the tweezer in a nonlinear force characterization experiment.

3.1
Experimental setup

At the starting point of our optical table, we have a Toptica DL-Pro continuous-wave laser operating at a wavelength of 780 nm. It emits a Gaussian beam with a power of approximately 39 mW, which is directed into a Toptica BoosTA tapered amplifier. The amplifier boosts the beam to a maximum output power of 1.55 W from a single-mode fiber. This fiber is subsequently collimated using a Thorlabs aspheric lens C260 TM-B, which has a focal length of 15 mm and a NA of 0.16. The collimated free-space beam that emerges has a waist W_0 of approximately 1.435 mm and a Rayleigh range z_R of 8.294 m, as measured using the knife-edge method.

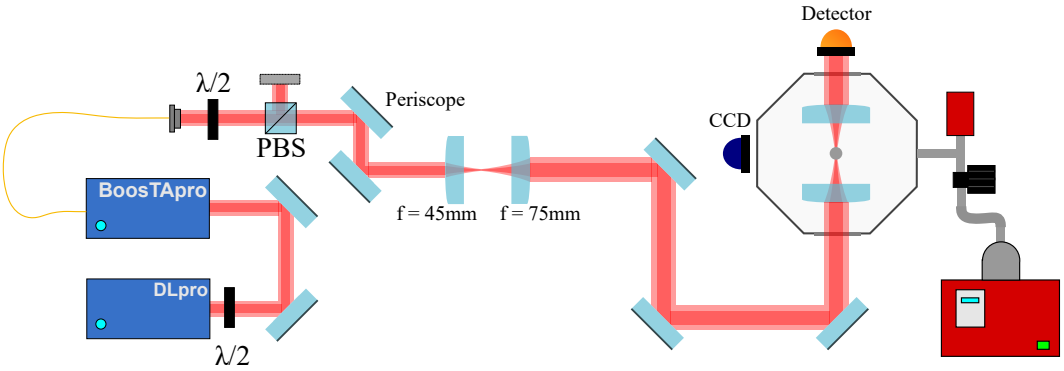

Figure 3.1: Schematic drawing of the optical setup for an optical tweezer in vacuum.

Continuing along the optical path, the beam traverses a $\lambda/2$ waveplate. This allows us to adjust its polarization before it meets a polarizing beam splitter (PBS). This setup affords us the ability to direct portions of the beam to different experimental stations on the optical table. For this specific

configuration, we use the horizontally polarized component of light, which is transmitted through the PBS.

Subsequent to the PBS, the beam navigates through a periscope system composed of a pair of Thorlabs E03 mirrors (common to all others in the setup). The purpose of the periscope is to elevate the height of the beam to match the vacuum chamber, and align it with the telescope that follows. This telescope is formed by coupling Thorlabs doublet lenses AC254-045-B and AC254-075-B, with focal lengths of 45 mm and 75 mm, respectively. The beam is expanded by a factor of 1.66, allowing it to fill an aspheric lens LightPath 355330 with a 5 mm diameter and lens focal ratio ($f/\#$) 0.65 that is located inside a vacuum chamber. Overfilling this lens is critical for ensuring the high NA of 0.77 that the lens offers. This configuration produces a tightly focused Gaussian beam, effectively forming the optical trap. An image of the tight focus can be seen in Fig-3.2.

Figure 3.2: Image of beam waist on the experiment, produced by the scattering of light by pure ethanol injected in the vacuum chamber.

To calculate the beam waist after passing through the tweezing lens, we must consider diffraction, a phenomenon that occurs when light passes through any aperture, like a lens, resulting in the creation of a pattern known as the Airy disk. This pattern has a central bright region surrounded by concentric rings of diminishing intensity. The Airy disk diameter ($\varnothing$), or minimum spot size, is approximated using [51]

$$\varnothing \approx 2.44 \times \lambda \times (f/\#), \tag{3-1}$$

where $(f/\#)$ is the lens f-number. For our lens, this yields a beam waist of $\approx 0.62\,\mu$m and Rayleigh range of $\approx 1.54\,\mu$m. These numbers will later be important to estimate the trap characteristics, like spring constant and frequencies of center-of-mass motion along the three directions.

Silica spheres from MicroParticles GmbH with a diameter of 143 nm are mono-dispersed in ethanol and introduced into the optical trap via a standard pharmaceutical nebulizer (Glenmark NebZmart). The particle aerosol is guided through from outside the vacuum chamber all the way to the trap center via a tube, producing a laminar flow and an atmosphere of particles around the trap. The typical drop radius produced by the nebulizer is less then $2.5\,\mu$m. The concentration used in most of our experiments is such that we have on average one particle per droplet of ethanol. With this system we are able to trap a particle in less than a minute. After a single particle is captured, the chamber pressure is slowly reduced to approximately 10 mbar. Images of a trapped particle can be seen in Figures 3.3 and 3.4

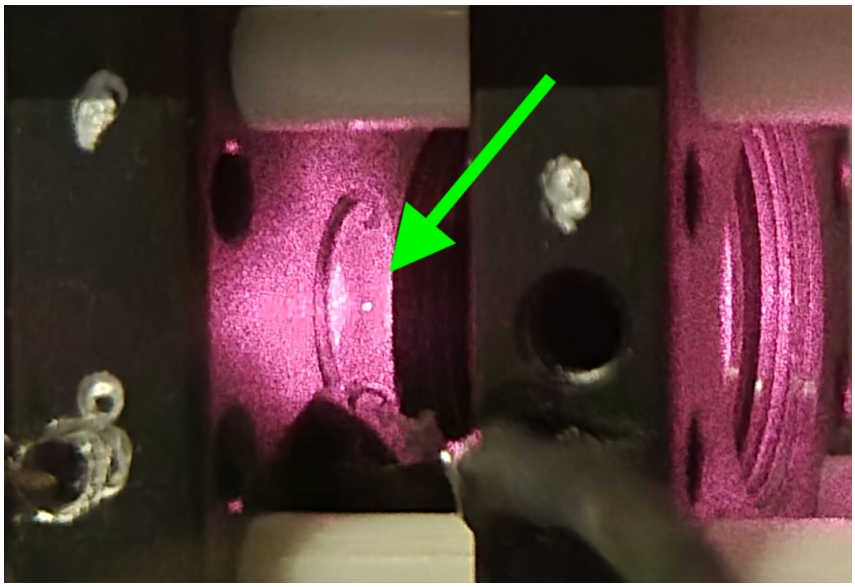

Figure 3.3: Image of scattered light from an optically trapped nanoparticle, captured with a smartphone.

The axial center-of-mass motion of the trapped particle, denoted as $z(t)$, is monitored by collecting forward-scattered light from the trapped particle. The scattered light is collected with an aspheric lens, and directed to a photodiode Thorlabs PDA100A2, which converts it into an electrical signal proportional to $z(t)$ and communicates with the oscilloscope TiePie Handyscope HS5. The oscilloscope is connected to the laboratory computer, where we have the voltage data recorded. A typical trace containing the information on the particle motion can be seen in 3.5. This data can be subsequently processed by Python.

Figure 3.4: Scattering light image of an optically trapped nanoparticle, captured using the lab's webcam post-imaging system.

Images of the particle are produced by collecting scattered light along the transverse plane, and directing such light to a CCD, also located outside the chamber.

Collecting the scattered light from the particle is crucial to achieving proper motion detection, since the forward scattered photons carry information on the particle's longitudinal position. The more photons we are able to collect, the more information we will have and the cleaner the signals corresponding to particle motion will be. Since the particle consists of a dispersive medium, it effectively alters the optical path of forward scattered photons and hence, the information is encoded in the phase of the scattered beam. Since non-scattered light travels together with the scattered beam, they automatically interfere, converting this phase information into an intensity information. A schematic illustration of this process can be seen in Fig-3.1. Choosing the proper collection lens is therefore crucial for an efficient motion detection; we do so by employing the methods described in [52]. As a result, theroetical graph of the efficiency versus NA of the collecting lens can be seen in Fig-3.6 with a peak at NA = 0.46. Based on this analysis, we chose to use a lens with an NA of 0.50, slightly deviating from the peak value but still within an efficient range. This choice aligns with our objectives for optimizing the optical setup.

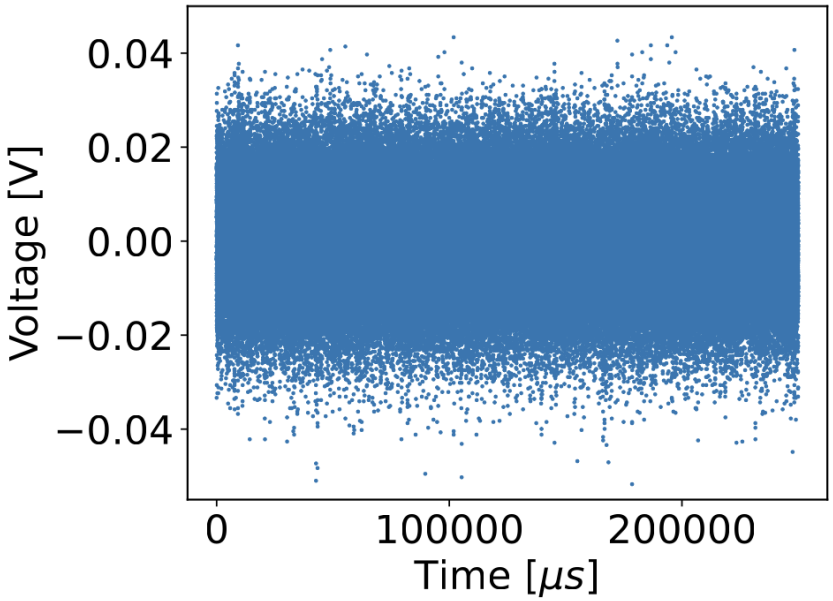

Figure 3.5: Voltage data from oscilloscope over 0.25 s at 1 MHz sampling frequency.

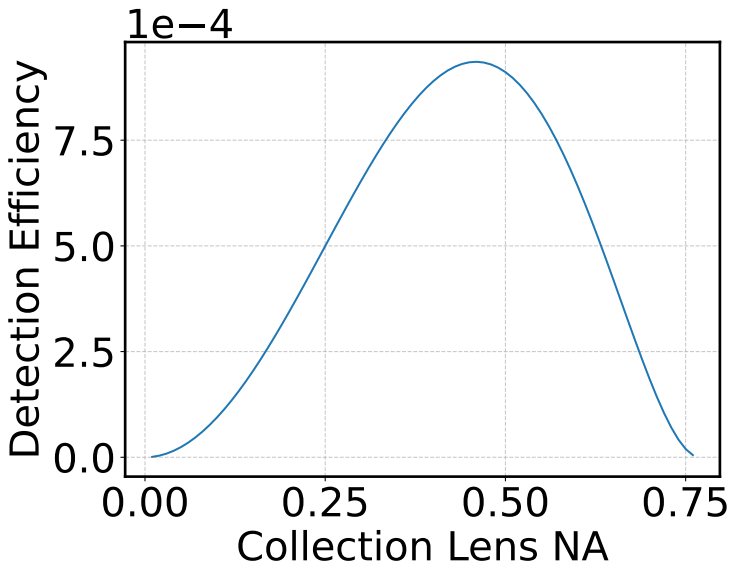

Figure 3.6: Graph to visualize the most efficient lens for forward detection.

3.1.1 Expected trap characteristics

In our experiment, we employ a beam power of approximately 240 mW. Consequently, without considering the scattering force, we obtain a potential depth of around $400\,\mathrm{k_B}T$ in the x, y directions and $600\,\mathrm{k_B}T$ in the z direction, as seen in Fig-3.7.

Despite neglecting the scattering force at this point, analysing the trap depth due to the gradient force indicates that longitudinal trapping is likely within reach with our experimental conditions. Indeed, the addition of the non-conservative scattering force shifts the equilibrium position, but as can be seen by the numerical simulations presented in the previous chapter, stable trapping can be successfully achieved.

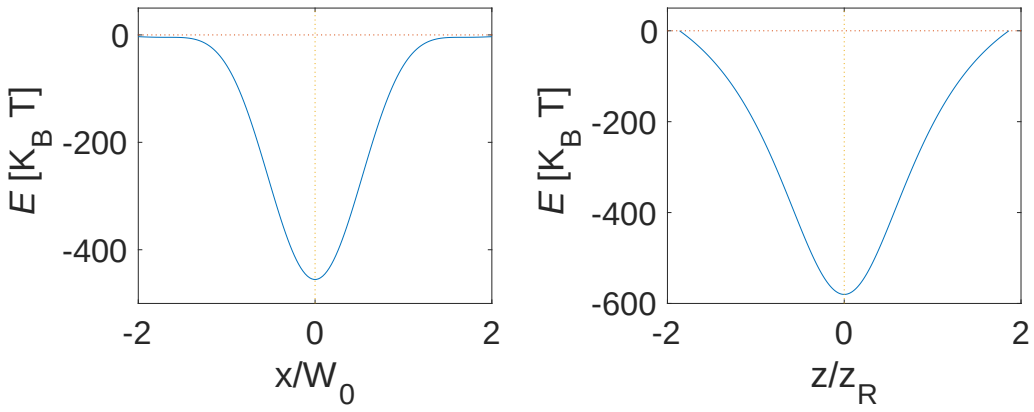

(a) Trap depth in x direction. (b) Trap depth in z direction.

Figure 3.7: Trap depth simulation considering only the gradient force.

It is also useful to estimate the frequencies for the motion along x, y and z directions expected in the experiment. Using Eqs. (2-29), (2-30) and the parameters described in the previous section we find the theoretical values for the trap stiffness and resonance frequency

$$k_z \approx 0.69\,\mathrm{pN}/\mu\mathrm{m} \rightarrow f_z \approx 72\,\mathrm{kHz} \tag{3-2}$$

$$k_{x,y} \approx 8.52\,\mathrm{pN}/\mu\mathrm{m} \rightarrow f_{x,y} \approx 253\,\mathrm{kHz}. \tag{3-3}$$

Compared to real data

$$k_z \approx 1.00\,\mathrm{pN}/\mu\mathrm{m} \rightarrow f_z \approx 89\,\mathrm{kHz} \tag{3-4}$$

$$k_x \approx 16.00\,\mathrm{pN}/\mu\mathrm{m} \rightarrow f_x \approx 348\,\mathrm{kHz} \tag{3-5}$$

$$k_y \approx 19.70\,\mathrm{pN}/\mu\mathrm{m} \rightarrow f_y \approx 385\,\mathrm{kHz}. \tag{3-6}$$

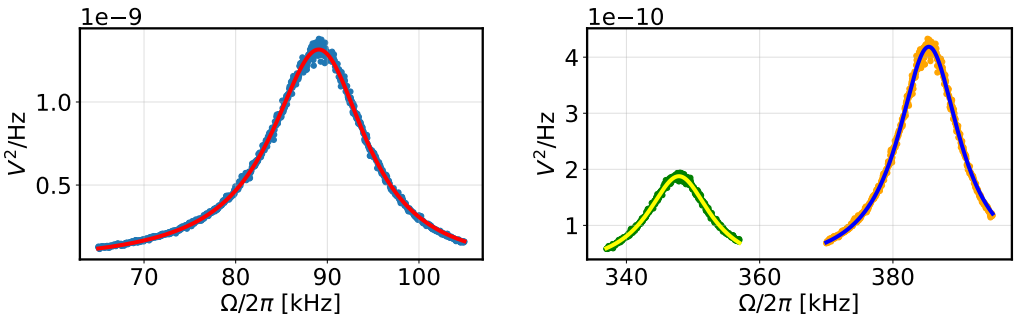

(a) z direction. (b) x and y directions.

Figure 3.8: Power spectral densities of a confined particle showing the resonance frequencies in the x, y and z directions. Lorentzian functions are fitted to the measured data yielding the central frequencies $\Omega_x/2\pi = 348\,\text{kHz}$, $\Omega_y/2\pi = 385\,\text{kHz}$, $\Omega_z/2\pi = 89\,\text{kHz}$.

These values are obtained by fitting Lorentzian functions to the PSDs in Fig-3.8, obtained from collecting traces of the particle motion. Note the theoretical values of the frequencies and trap stiffness are on the same order of magnitude as the experimental ones.

Another important parameter is the tweezer's spring constant, which is a measure of how much force must be applied to the particle in order to displace it by a certain amount of length. Typical spring constants are on the order of $1\,\text{pN}/\mu\text{m}$ to $10\,\text{pN}/\mu\text{m}$, indicating that we need approximately $1 \sim 10\,\text{pN}$ to move the particle by $1\,\mu\text{m}$. By the equipartition theorem, the mean squared deviation of the longitudial particle position is $\langle z^2 \rangle \approx k_B T/2$, corresponding to $\sqrt{\langle z^2 \rangle} \approx 1\,\text{nm}$. This means that the force fluctuations in the experiment are on the order of $\delta F \approx k_z \sqrt{\langle z^2 \rangle} \approx 0.001\,\text{pN}$, which implies the particle can be used as a force sensor with a minimum sensitivity of approximately δF.

3.2 Application

Traditional experiments often involve a dielectric particle trapped in a tightly focused Gaussian beam, which usually approximates a confining harmonic potential. The particle undergoes Brownian motion due to its interaction with the surrounding medium, and measuring its position correlation functions and associated power spectrum allows for a characterization of the trap's parameters [49].

Recently, the study of nonlinear optical tweezers has gained prominence [37, 39]. By employing beams with complex intensity profiles, like double-well landscapes [35, 36], the optical potential experienced by the particle becomes

inherently nonlinear, differing from the typical harmonic potential commonly found in optical levitation experiments. Engineering potential landscapes that go beyond the harmonic approximation is increasingly vital for applications such as non-equilibrium Brownian machines [17], the preparation of non-classical and non-Gaussian quantum states [53], and matter wave interference experiments [54]. As a result, the behavior of trapped particles deviates from simple harmonic motion [33], requiring a more sophisticated analysis using nonlinear stochastic differential equations to understand the particle's motion correlation functions and power spectrum.

The present application aims to experimentally validate a theoretical framework presented in [33] by implementing effective nonlinear potential landscapes on a levitated particle using electric feedback forces. This method implies corrections to the statistical moments of particle motion to be computed, particularly the position power spectrum, opening new pathways for understanding nonlinear dynamics in optical trapping.

3.2.1 Experiment

A simplified schematic of the experimental setup is shown in Fig-3.9. The configuration is similar to the one described previously in Sec-3.1, but with modifications to be able to implement nonlinear position-dependent forces upon a levitated nanoparticle.

The motion of the center-of-mass of the confined particle, denoted as $z(t)$, is detected by capturing forward scattered light. The detected signal is passed through a wide band-pass filter, amplified and then fed into an FPGA (*Field-Programmable Gate Array*) - a specialized integrated circuit designed to process the signal received from the detector. This circuit subsequently produces a voltage, generating a force on the particle that's relative to $z^3(t-\tau)$ and a certain feedback gain. Here, τ is the total electronic delay originated by the electronic system.

To implement an electric field near the confined particle, a pair of electrodes is positioned in the trapping and collecting lenses mounts. These electrodes are linked to both a signal filter and an amplifier, found before and after the FPGA, including the FPGA itself. As a result, an electric force is established at the particle's location, described by $G_{fb}z(t-\tau)^3$, where G_{fb} is the net feedback gain output from the combined efforts of the FPGA and amplifier.

We proceed to verify the perturbation theory as described in [33]. We apply an effective quartic potential (cubic perturbation force) on the trapped particle

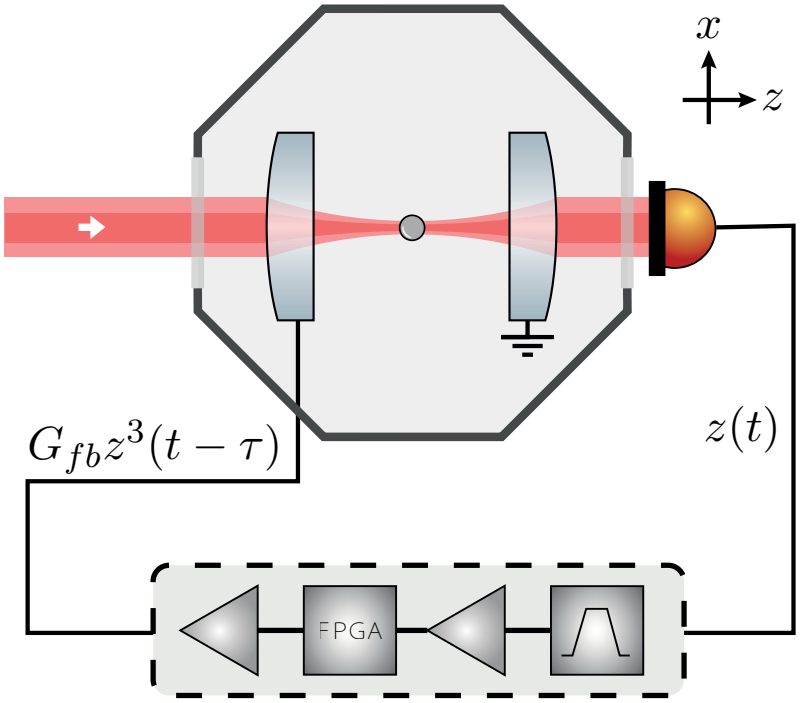

Figure 3.9: Experimental setup. A silica nanoparticle is trapped by an optical tweezer in vacuum. The forward scattered light is collected and sent to a photodiode, producing a signal proportional to the particle's axial coordinate, $z(t)$. An FPGA processes the signal to produce a voltage that induces a force on the trapped particle proportional to $z^3(t-\tau)$. Amplification prior to and after the FPGA enhance the maximum resolution of its analog-to-digital converter, enabling the exploration of a broader range of values for the applied electrical force.

generated via the position measurement feedback as described previously. This is valid for small G_{fb},

$$G_{fb} \ll \frac{m^2\omega_0^4}{2k_bT_{\text{eff}}}. \tag{3-7}$$

PSD's of particle motion under the influence of the cubic feedback force with positive and negative feedback gains can be seen in Fig-3.10(a). These measurements qualitatively confirm the effect of the cubic force predicted by perturbation theory as a shift in the PSD central frequency ($\Delta\Omega$) given by

$$\frac{\Delta\Omega}{2\pi} = \frac{3k_bT}{4\pi m^2\omega_0^3}G_{fb} \equiv \kappa G_{fb}, \tag{3-8}$$

where ω is the angular resonance frequency.

Note that the shift depends on the sign of the feedback gain, in accordance to Eq. (3-8), indicating an effective hardening or softening of the optical trap due to the cubic actuation.

To quantitatively compare the frequency shifts with the prediction from

perturbation theory, we acquired the longitudinal motion PSD for different values of feedback gain G_{fb}. Fitting Lorentzian functions to the PSDs we obtained the central frequency as a function of feedback gain. The result of these measurements is shown in Fig-3.10(b), in comparison to the theoretical prediction given in Eq. (3-8) for our experimental parameters. Good agreement between the data and the theoretical prediction was observed within the perturbation regime, indicated by the non-shaded region of the plot. Note also that outside the regime of perturbation theory (grey shaded regions in Figure 3.10b)), the measured shifts fall systematically slightly bellow the predicted first order correction, consistent with the second-order correction scaling of $\mathcal{O}(G_{fb}^2)$ [33]. Finally, the experimentally obtained angular coefficient κ_e was measured to be

$$\kappa_e = (5.46 \pm 0.10) \times 10^{-4}\,\mathrm{Hz\,m^3\,N^{-1}} \tag{3-9}$$

which compares to the theoretical prediction given the parameters for our experiment,

$$\kappa_t = 5.69 \times 10^{-4}\,\mathrm{Hz\,m^3\,N^{-1}}\ . \tag{3-10}$$

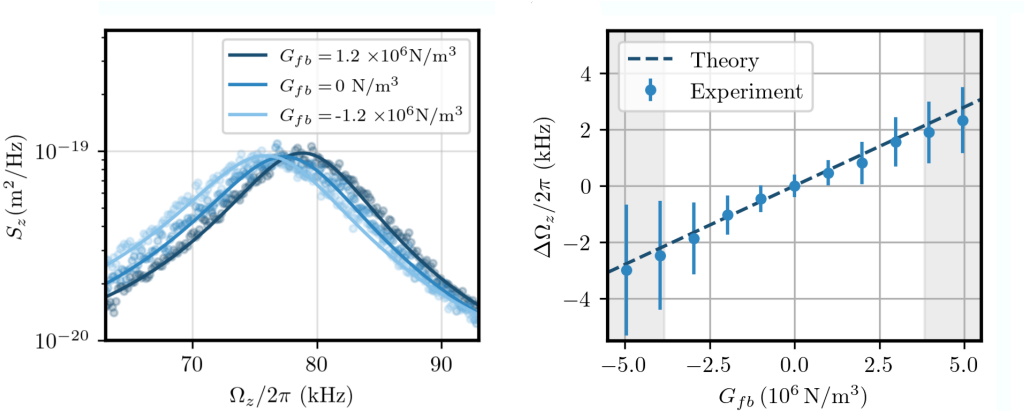

(a) PSDs of the trapped particle's longitudinal motion under cubic force, displaying central frequency shifts. The data was taken at 293 K and a pressure of 10 mbar. The reference PSD has a central frequency of 77.8 kHz and a shift of ±1.4 kHz was measured for $G_{fb} = \pm 1.2 \times 10^6$ N/m^3.

(b) Frequency shifts as a function of G_{fb}, verifying the prediction of perturbation theory given by Eq. (3-8) (dashed line). The grey shaded region marks the regime of validity for perturbation theory described in Eq. (3-7). Each point corresponds to 250 seconds of data acquisition at 500 kHz divided into 1000 traces and organized into batches of 5 traces each. All data points were collected using the same nanoparticle.

Figure 3.10: Verifying the predictions of perturbation theory

3.2.2 Conclusion

In summary, a cubic nonlinear force derived from position measurement feedback has been applied to an underdamped levitated nanoparticle. We examined the impact of this force on the particle's random behavior through experiments. Specifically, we measured the changes in the particle's motion power spectrum induced by the cubic feedback force and found them to be consistent with existing path integral perturbation theory for nonlinear optical tweezers.

We expect that nonlinear feedback methods will be useful in various levitodynamics experiments, both in classical and quantum settings. Such feedback-induced forces can be used for state preparation that goes beyond the inherent nonlinearities in optical potentials [54, 55]. Additionally, delayed nonlinear feedback can be employed to create systems with specific types of nonlinear damping [56].

4
Structured light vacuum optical tweezer

Conventional optical trapping techniques, using Gaussian laser beams, provide a hamonic potential to a good approximation [45]. As we have seen, 'standard' optical tweezers can serve as very good force and displacement sensors [57], but they do not explore the full capabilities offered by light. As we also discussed earlier, electromagnetic waves can be shaped into various transverse spatial profiles using the superposition of higher-order modes (Laguerre-Gauss or Hermite-Gauss, for example). With these *structured light* modes, we can engineer the field gradients, and consequently design novel types of optical traps [37, 58]. For instance, we could engineer a stiffer trap, a non-linear trap, and perhaps most interestingly, a multi-particle trap. It is the purpose of this chapter to deal with these structured optical traps. This chapter dives into an innovative approach that involves the use of structured light in vacuum optical tweezers to address these challenges.

To produce structured light beams, we employ a device called *Spatial Light Modulator* (SLM). It consists in a sort of variable grating, capable of modulating the phase of an incoming beam in an essentially arbitrary spatially varying pattern [59]. As a consequence, we are able to shape the transverse profile of the beam, producing the desired mode superposition.

In what follows we will briefly describe principles of functioning of the SLM and holographic beams generation, as well as practical details on how to calibrate it. Subsequently, we describe an experimental setup where general structured light optical traps can be implemented. We use this setup to implement a special beam, known in the literature as the optical bottle beam (OBB) [37, 38, 60].

The OBB is an interesting choice of structured light for optical trapping since it has two intensity maxima along the longitudinal direction. We could imagine, therefore, trapping two neighbouring particles in each of these maxima, opening the possibility of studying multi-particle levitated optomechanics in vacuum [39].

After discussing some properties of the OBB, we report initial attempts at multi-particle trapping in the OBB and results on the trapping of single and clusters of Silica nanoparticles.

4.1 Spatial Light Modulator

In our laboratory, we generate structured light modes using the SLM (HOLOEYE Photonics, model PLUTO-NIR-015 HR). The special interest to us are the Laguerre-Gauss modes, described in Chapter 2. This device consists in a 1920×1080 pixel electronic display (*Liquid Crystal on Silicon* micro-display - LCOS), where each pixel is an individually adjustable liquid crystal cell to effectuate alterations in the electric field of an incoming light beam. The uniform amplitude of an incoming laser beam can be modulated by introducing a phase delay $\phi = \phi_1(x, y)$, where (x, y) are the coordinates on the hologram, of 0 or π on the liquid crystal (LC) pyxels with the use of ferroelectric modulator [59].

The LCOS micro-display consists of several layers: cover glass, transparent electrode, alignment layer, liquid crystal layer, another alignment layer and the *complementary metal-oxide-semiconductor* (CMOS) with a refractive layer. When the display is activated, a voltage is applied pixel-wise between the CMOS and transparent electrode layers.

The phase modulating capability of the setup is derived from the combined electrical and optical anisotropy of LC material. Specifically, the dipole nature of the LC (electrical anisotropy) allows for a varying orientation of the LC molecules based on the strength of the applied electric field. Furthermore, the LC molecules exhibit birefringence, meaning they have different refractive indexes for their perpendicular molecular axes (optical anisotropy).

Together, these properties enable the retardation or phase modulation of light waves. Each SLM pixel can receive a distinct voltage, resulting in a unique phase delay. In practice, the display is addressed using an 8-bit grayscale bitmap image, where each gray level corresponds to a specific mean voltage across the LC layer at that pixel. For the generation of an LG mode, it is essential for a horizontally polarized Gaussian Beam to strike the LCOS. Once the screen is appropriately programmed, it presents a phase pattern corresponding to the 2D Laguerre-Gauss equations and the result can be seen in Fig-4.1.

We should include a tilt function $\tau(x, y) = m_x x + m_y y$ to the phase function $\phi(x, y)$ in order to separate the undiffracted order 0 to higher orders. In this context, $m_x x$ and $m_y y$ determine the tilt magnitude along x and y directions respectively.

The complex uniform amplitude of the object beam $A(x, y)$ can be written as

$$A(x, y) = \exp(i\Phi(x, y)), \tag{4-1}$$

where

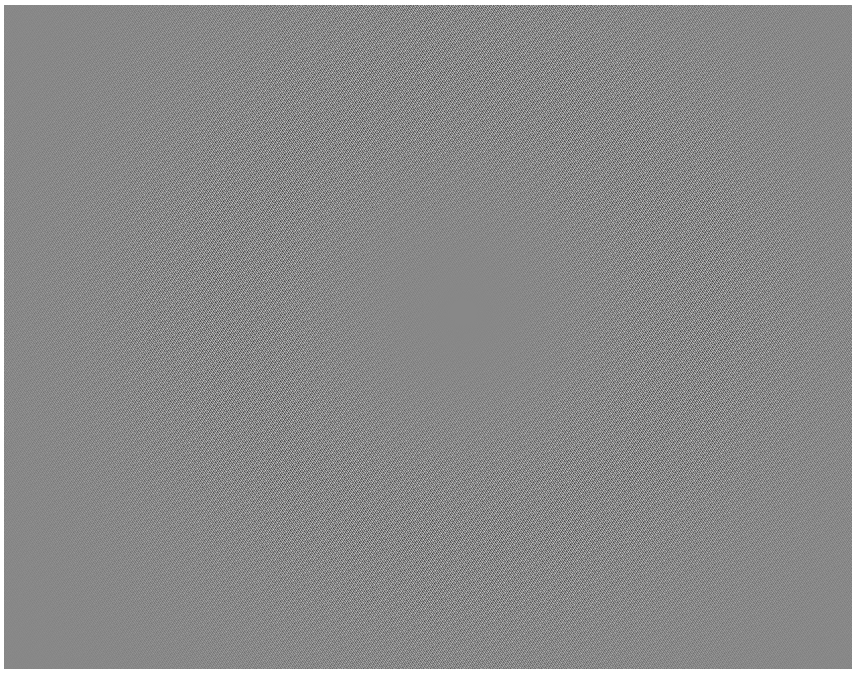

Figure 4.1: SLM hologram pattern for producing an $LG_{0,2}$ mode

$$\Phi = \phi(x, y) + \tau(x, y). \tag{4-2}$$

The beam's corresponding binary hologram transmittance, $t(x, y)$, is defined as

$$t(x, y) = \begin{cases} 1, & \text{if } \cos\Phi(x, y) \geq 0 \\ 0, & \text{otherwise.} \end{cases}$$

When visualised, $t(x, y)$ behaves like a square wave in relation to $\Phi(x, y)$, leading to its Fourier expansion

$$\begin{aligned} t(x, y) = \frac{1}{2} + \frac{1}{\pi}\Big[& \exp(i\Phi) + \exp(-i\Phi) \\ & - \frac{1}{3}\left(\exp(3i\Phi) + \exp(-3i\Phi)\right) \\ & + \frac{1}{5}\left(\exp(5i\Phi) + \exp(-5i\Phi)\right) + \cdots \Big]. \end{aligned} \tag{4-3}$$

Considering the backfocal plane of the first lens, the diffraction pattern of $t(x, y)$ is

$$T(f_x, f_y) = \int_{-\infty}^{\infty} \int t(x, y) \exp\left(-2\pi i(xf_x + yf_y)/\lambda f\right) dxdy, \tag{4-4}$$

Here, (f_x, f_y) stands for backfocal plane coordinates, λ for the beam's wavelength, and f the focal length of the first lens after the SLM display. The diffraction pattern $T(f_x, f_y)$ serves as the Fourier transform of $t(x, y)$. Each

term in the equation corresponds to various spatial orders in the Fourier plane due to different τ tilts.

The diffraction orders $(\pm 1, \pm 2, \pm 3, \cdots)$ have phase information of $(\pm 1, \pm 2, \pm 3, \cdots)\phi(x, y)$. In our case, the 1^{st} order diffraction term is isolated and transmitted to the second lens.

Figure 4.2: LabView software used to calibrate the SLM and create the beam superposition. Program courtesy of the Quantum Optics Group at Universidade Federal Fluminense.

We empirically calibrate the diffraction settings to obtain a well-defined mode with the software LabView (left image in Fig-4.2). There, we have to input values for deviation angle in x-z plane, that determines horizontal distance between the diffraction orders in a transverse plane. Higher the value of x-z , higher the distance between the modes; the y-z angle, who is responsible for vertical distances; and consider the blazing configuration showed (right image in Fig-4.2). This fine adjustment improves the fraction of total power that is transmitted for a specific order of propagation.

4.2 Optical Bottle Beam

Utilizing the SLM, we create a beam superposition that combines the Gaussian beam $LG_{0,0}$ with $LG_{p,0}$ where $p = 1$, incorporating a relative phase of π. This superposition is specifically chosen to produce a beam characterized by two distinct potential wells, as shown in Fig-4.5. Its electric field is

$$\vec{E}^{OBB}(\rho, z) = E^G - E^G L_1^0 \left(\frac{2\rho^2}{W(z)^2} \right) \exp[-2i\zeta(z)]\ \hat{\epsilon} \tag{4-5}$$

where $\hat{\epsilon}$ is the polarization vector. The corresponding intensity of the OBB is

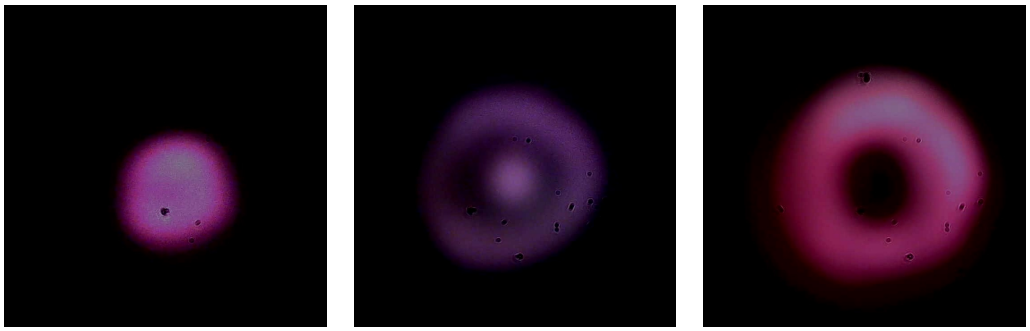

Figure 4.3: Images of the OBB transverse profile along the propagation axis.

$$I^{OBB}(\rho,z) = I_0\left(\frac{W_0}{W(z)}\right)^2 \exp\left[-\frac{\rho^2}{W^2(z)}\right] \times \\ \times\left[1-2\cos\left(2\arctan\frac{z}{z_R}\right)L_1^0\left(\frac{2\rho^2}{W(z)^2}\right)+L_1^0\left(\frac{2\rho^2}{W(z)^2}\right)^2\right]. \tag{4-6}$$

In Fig 4.4 we plot the intensity profile along the x and z directions.

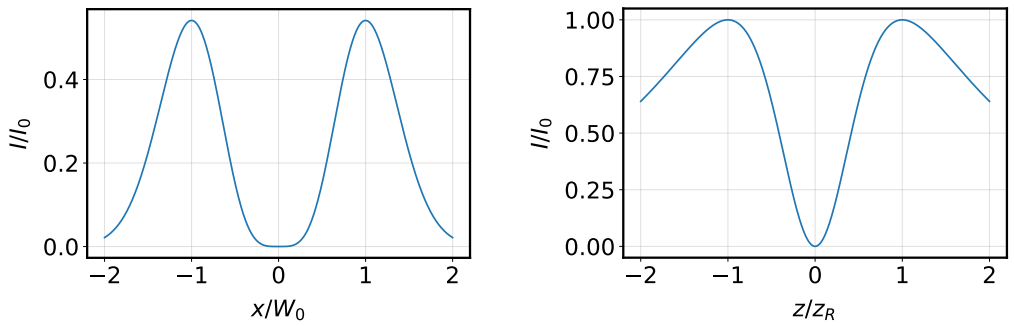

Figure 4.4: OBB intensity profile on x and z directions.

We note that alternative optical bottle beams can be generated using higher order modes, for instance a LG mode with $p = 2$ [60]. However, the choice of $p = 1$ is motivated by two factors that influence the practicality of trapping two particles. First, the SLM is considerably less efficient at generating higher-order modes, making $p = 1$ the most practical choice for optical tweezers. Second, the choice of p influences the separation between the intensity maxima, where trapped particles are expected to be; higher p values would result in less distance between two neighbour particles. Since we expect the neighbouring particles will mutually interact, for instance via Coulomb interaction, coherent scattering and optical binding [61, 62], we expect it to be more challenging to achieve multi-particle trapping with closer separations, resulting in higher interaction forces described in [39].

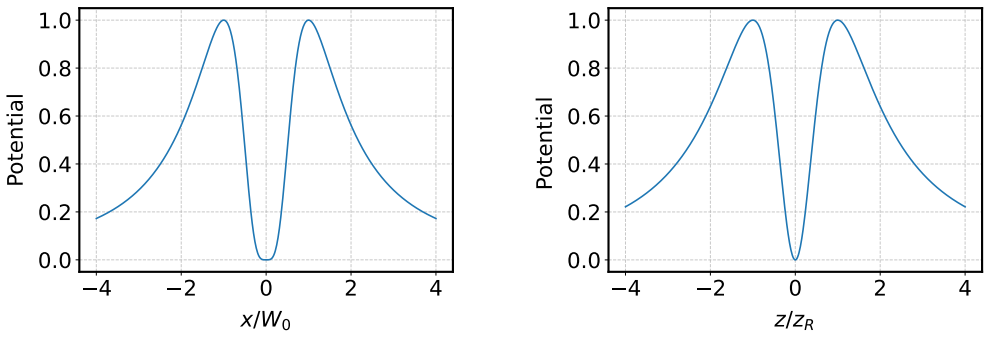

Figure 4.5: OBB normalized potential profiles in x and z directions.

4.3 Setup

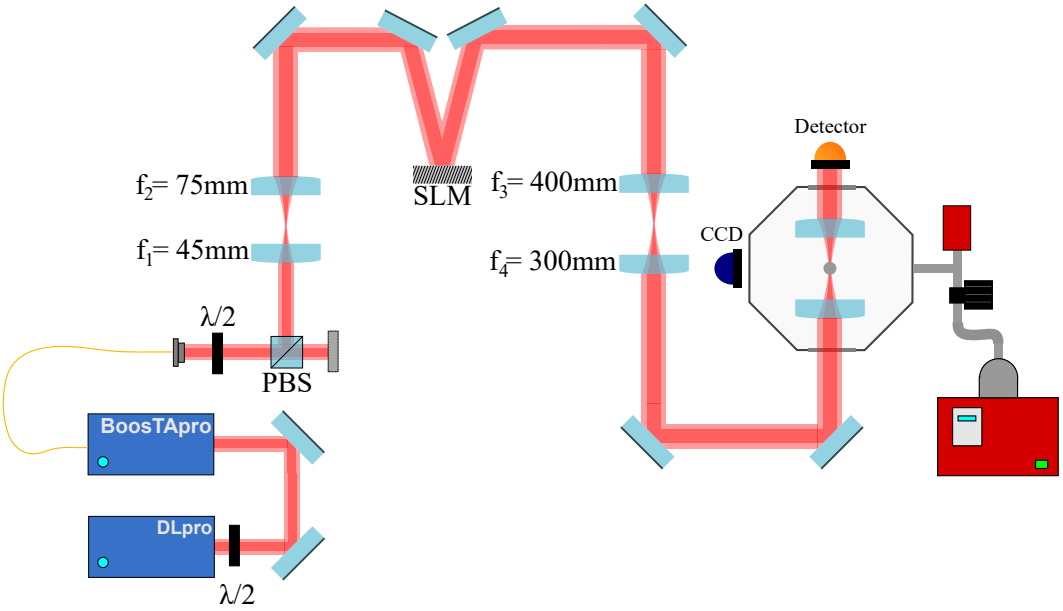

Figure 4.6: Schematic drawing of the optical setup for the structured light trap in vacuum.

The strucutured light optical trap setup is similar to the one described in Section 3.1, up to the point where the beam reaches the PBS. In this particular experiment, we utilize the beam that is reflected from PBS. The beam subsequently passes through a telescope, composed of lenses with focal lengths of 45 mm and 75 mm. This configuration results in a magnification factor of 1.66, producing a beam with a radius of 2.39 mm. The beam is then steered by a pair of dielectric mirrors (Thorlabs BB1-E03), which are deliberately tilted to direct it onto the SLM display. This slight tilt aids in separating the n^{th}-order diffraction modes from the 0^{th}-order mode. Among the modulated beams, the one of interest is the 1^{st}-order mode immediately succeeding the

0^{th}-order mode, which also happens to be the second strongest. Any remaining unwanted modes are filtered out to prevent undesirable interference.

The modulated beam subsequently traverses a $4F$ system, comprised of two lenses. The first lens (Thorlabs AC254-400-B) has a focal length $f_3 = 400\,\text{mm}$ and is positioned at a distance equal to its back focal length of 391.1 mm from the SLM display. The second lens (Thorlabs AC254-300-B) has a focal length $f_4 = 300\,\text{mm}$ and is placed at a distance equal to the sum of its own back focal length (290 mm) and that of the first lens (391.1 mm). Between the two lenses, the beam passes through a periscope, to match the height of the vacuum chamber.

After the telescope, the beam encounters another $\lambda/2$ waveplate and a PBS. These components are included for the purpose of establishing a back-detection scheme, which is yet to be implemented, and to calibrate the SLM, as we put a CCD in the direction of the reflacted beam to analyse the beam shape. Finally, the beam goes towards two alignment mirrors and passes through the same optical trapping system as described in Section 3.1. The high NA lens is precisely positioned at the focal length of the second lens, completing the $4F$ system.

With this setup, we can in principle generate arbitrary structured light modes for optical trapping. To demonstrate this capability, we trap the particle using the OBB mode. To do so, we initially configure the SLM to generate a Gaussian beam pattern. Employing the Gaussian beam offers advantages in terms of both the potential well and the SLM's efficiency, making it easier to capture the nanoparticle using the previously described nebulizer drop-off system. Once the particle is levitated at the focal point, we transition the beam to an OBB mode with $p = 1$. At this stage, the Gaussian focal point is replaced by a ring-shaped beam. Additionally, new potential wells are formed at distances z_R and $-z_R$ (or $0.4\,\mu$m and $-0.4\,\mu$m) from the focal point, effectively creating a double potential well. As we switch the SLM parameters from the Gaussian to the OBB mode, the particle relocates to one of these new wells. With this technique we were able to succesfully trap a particle using the OBB mode with strctured light and even achieve a vaccum of 1 mbar.

For technical reasons associated with the SLM, the maximum power achievable in our optical tweezer setup varies depending on the beam mode in use. Specifically, with the Gaussian mode, we are able to attain a peak power of 260 mW, while in the OBB (Optical Bottle Beam) mode, the maximum power is limited to 160 mW. This creates a potential depth of around $500k_BT$ for the Gaussian beam and $250k_BT$ for the OBB, considerably smaller.

For the specific application discussed in Section 3.2, a concentration of

one silica (SiO_2) nanosphere per droplet of ethanol was used. In contrast, the aim for the current experiment is to achieve dual-particle trapping, requiring a concentration of two nanospheres per droplet. There are two main factors that support our hypothesis that dual-particle trapping is feasible. First, the size of the potential well decreases when the trapping mode is switched from Gaussian to OBB mode. This reduced well size indicates that it is less likely for two particles to occupy the same spatial region, effectively making it more challenging for both to 'fit' into the same trapping site. Second, electrostatic repulsion between the charged particles is expected to segregate them into separate potential wells, further facilitating the dual-particle trapping strategy in different spots.

4.4 Results

We successfully trapped a particle with the OBB. Now, it's essential to cross-check the trap parameters of the particle confined within the OBB to confirm that our theoretical predictions match the actual experimental results. For this validation, we adopt an approach analogous to the one used for the Gaussian beam. We expand Eq. (4-6) into a Taylor series to determine the central frequency of motion using the OBB. For the z direction, we expand around the point (ρ, z_R), where the intensity distribution exhibits a Gaussian profile and is the position where our particle will be trapped.

$$\begin{aligned} I_z(\rho,z) \approx & \frac{I_0 e^{-\frac{\rho^2}{2W_0^2}}}{16W_0^8 z_R^2}\Big(4\rho^2 W_0^6\left(z^2+4zz_R-9z_R^2\right)+2\rho^4 W_0^4\left(25z^2-66zz_R+45z_R^2\right) \\ & -4\rho^6 W_0^2(4z-5z_R)(z-z_R)-16W_0^8 z(z-2z_R)+\rho^8(z-z_R)^2\Big). \end{aligned} \tag{4-7}$$

And for the x-y directions, expanding in (ρ, z) gives

$$I_\rho(\rho,z) \approx \frac{4I_0 z^2 z_R^2}{(z^2+z_R^2)^2} - \frac{12I_0 z^2 z_R^4 \rho^2}{W_0^2(z^2+z_R^2)^3} \tag{4-8}$$

Taking the derivative of Eq. (4-7) and (4-8) into Eq. (2-24), substituting to values $(0, z)$ and (ρ, z_R) respectively and ignoring the constant term results in

$$\begin{aligned} k_z &= \frac{2\pi n_m R^3}{c}\left(\frac{m^2-1}{m^2+2}\right)\left(\frac{2I_0}{z_R^2}\right) \\ &= \frac{2\pi n_m R^3}{c}\left(\frac{m^2-1}{m^2+2}\right)\frac{4P}{\pi W_0^2 z_R^2} \end{aligned} \tag{4-9}$$

$$k_x = k_y = \frac{2\pi n_m R^3}{c}\left(\frac{m^2-1}{m^2+2}\right)\left(\frac{3I_0}{W_0^2}\right) = \frac{2\pi n_m R^3}{c}\left(\frac{m^2-1}{m^2+2}\right)\left(\frac{6P}{\pi W_0^4}\right) \tag{4-10}$$

Different from the Gaussian tweezer setup, in this case there is no overfilling of the lens, thus our NA is not 0.77 as the maximum provided. This creates a smaller trapping stiffness and, consequently, smaller resonance frequencies values. Another point that the trap stiffness and frequency smaller is the power, as it can't be as high as with the Gaussian beam by experimental reasons described in the next section. With this in mind, considering a NA = 0.70 and power of 150 mW,

$$k_z \approx 0.21\,\mathrm{pN}/\mu\mathrm{m} \rightarrow f_z \approx 40\,\mathrm{kHz} \tag{4-11}$$

$$k_{x,y} \approx 2.38\,\mathrm{pN}/\mu\mathrm{m} \rightarrow f_{x,y} \approx 134\,\mathrm{kHz} \tag{4-12}$$

Compared to measured data verified by the plot in Fig-4.7 with the same parameters

$$k_z \approx 0.13\,\mathrm{pN}/\mu\mathrm{m} \rightarrow f_z \approx 31.4\,\mathrm{kHz} \tag{4-13}$$

$$k_{x,y} \approx 4.65\,\mathrm{pN}/\mu\mathrm{m} \rightarrow f_{x,y} \approx 187\,\mathrm{kHz} \tag{4-14}$$

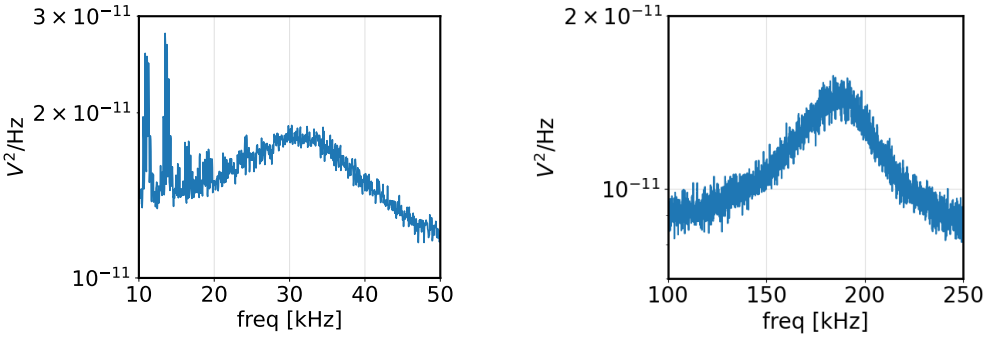

(a) Resonance frequency on z.

(b) Resonance frequency on x and y.

Figure 4.7: Resonance frequency of a trapped particle on x, y and z directions.

Utilizing the SLM with a Gaussian mode enabled the observation of different resonance frequencies within the same particle and pressure by varying the power, as depicted in Fig-4.8.

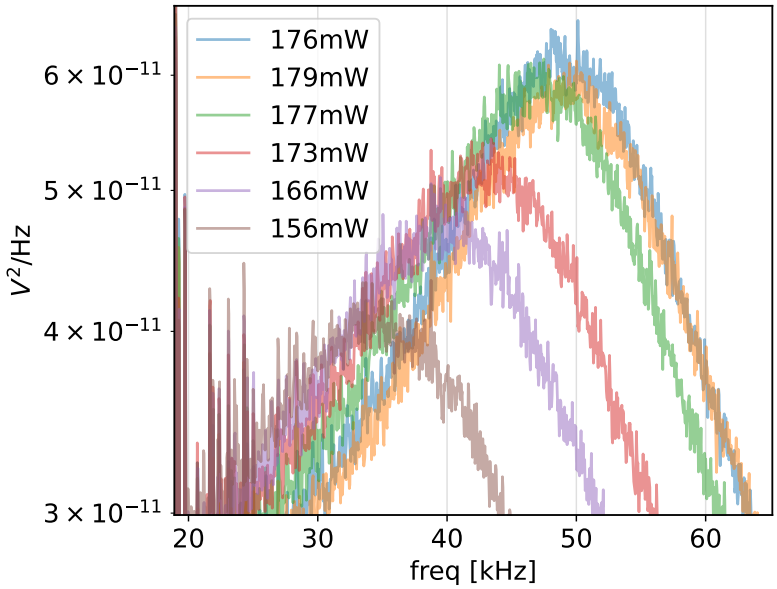

Figure 4.8: Resonance frequencies of a trapped particle on a Gaussian beam at different power values.

In the experiment, a consistent difference in light intensity was observed when varying the concentration between one and two particles per droplet. The light intensity is noticeably greater with the higher concentration compared to the lower concentration. This occurrence suggests that the potential well can retain more than one particle. An image of this event can be seen in Fig-4.9.

One of the challenges in trapping particles with the OBB arises from the noise in the SLM, which was observed after a meticulous analysis and can be seen in Fig-4.10. This results in a challenge when observing the PSD of the trapped particle, as it gets submerged beneath this noise. If two particles are trapped, each in a distinct potential well, detection and analysis would be problematic due to the limited resolution of our camera and the cumbersome PSD analysis.

A potential solution could be the incorporation of new pair of lenses for the $4F$ system that can better fulfill the trapping lens requirement and attain a higher NA, or by adopting a more efficient model of SLM that can augment stiffness, thus causing the frequency to shift to the right, or that doesn't exhibit this type of noise anymore. An alternative solution that doesn't involve more power of better NA could be utilizing a balanced detector; one end receives only the noise without the SLM and the other end receives the noise plus the PSD of the trapped particle, thereby allowing the noise to be mitigated by subtracting one from the other; or by inserting an $\lambda/2$ waveplate and PBS before the tweezing lens, implementing this way a backward detection, noticible to be more efficient [52]. Implementing backward detection is intriguing as it

(a) Low intensity scattered light from trapped particle.

(b) High intensity scattered light from trapped particle.

Figure 4.9: Different light intensities from trapped nanoparticle that could indicate multiple particles being trapped in b).

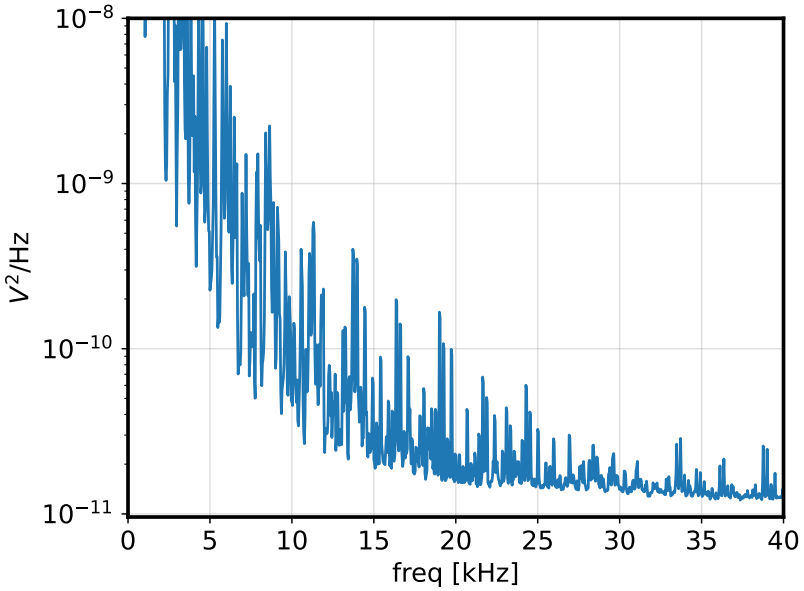

Figure 4.10: Noise caused by the SLM. PSD taken without particle.

may also yield information about the distance between particles. This is because the backward scattered light from the more distant particle can interfere with that from the closer one, creating a signal that is proportional to the distance between them.

Nonetheless, detection on the x and y directions avoids the issue of being too close to the SLM noise. The PSD in Fig-4.11 was taken from a Gaussian beam modulated by the SLM. It shows different peak positions, with two well separeted and one with a flat top, possible caused by two peaks very approximated, and that can be explained by a cluster of particles as represented

in [63].

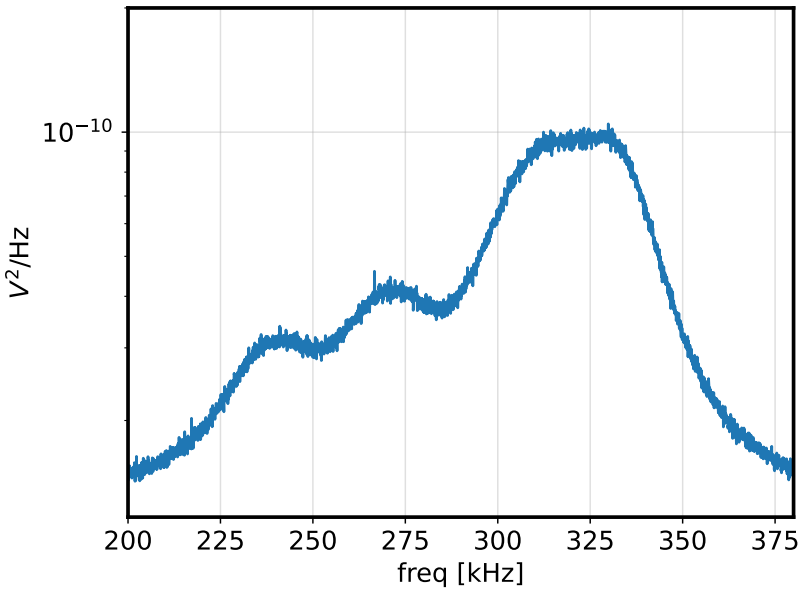

Figure 4.11: PSD of apparent cluster of particles.

.

5
Conclusion and outlook

Over the course of approximately two years, the work described in this thesis helped assembling a general-purpose vacuum tweezer experimental setup. This required careful micro-metric precision alignment, and resulted in an on-demand, stable vacuum optical trap which can now be employed in various experiments. It is worth mentioning that, to the best of our knowledge this has been the first vacuum optical tweezer for silica nanoparticles in Brazil. Two initial experiments were conducted with the tweezer, one complete, and the other in ongoing development.

The complete experiment consisted in a detailed study of the effect of non-linear forces in the stochastic motion of a Brownian particle within the perturbation regime. This study used a cubic nonlinear electric feedback force to analyze alterations in the stochastic behavior of an underdamped levitated nanoparticle, specifically measuring the changes in the particle's position power spectrum. The findings confirm previous theoretical predictions for nonlinear optical tweezers [33]. The nonlinear feedback methods employed in this work can be used as a resource for quantum state preparation beyond the intrinsic nonlinearities present in standard optical potentials and for nonlinear damping and control in both classical and quantum regimes.

For the ongoing experiment, we have setup a modified version of the vacuum tweezer, connected now to a spatial light modulator for producing structured light modes of the trapping beam. In particular, we have showed that a particle trapped in a standard Gaussian tweezer can be successfully transferred to a structured light mode, i.e. the optical bottle beam in vacuum. Trapping in the bottle beam is interesting, as it has two neighbour intensity maxima along the beam propagation, opening the possibility of trapping pairs of particles at a close distance on the order of a micron. Once stable trapping of particle pairs is successfully achieved, a myriad of possibilities opens in terms of physics experiments. We could for instance study particle interactions, from Coulomb to coherent scattering and optical binding, as well as multi-particle cooling schemes via feedback of the optical trap and applied electric field. This set the stage for multi-particle quantum optomechanics, which in the future could lead to tests of quantum mechanics in new scales.

Bibliography

[1] A. I. Sabra, *Theories of light: from Descartes to Newton*. Cambridge University Press, 1981.

[2] R. A. Beth, "Mechanical detection and measurement of the angular momentum of light," *Physical Review*, vol. 50, no. 2, p. 115, 1936.

[3] E. F. Nichols and G. F. Hull, "The pressure due to radiation," in *Proceedings of the American Academy of Arts and Sciences*, vol. 38, no. 20. JSTOR, 1903, pp. 559–599.

[4] T. H. Maiman *et al.*, "Stimulated optical radiation in ruby," 1960.

[5] A. Ashkin, "Atomic-beam deflection by resonance-radiation pressure," *Physical Review Letters*, vol. 25, no. 19, p. 1321, 1970.

[6] S. Chu, "Observation of a single-beam gradient force optical trap for dielectric particles," *Optics letters*, vol. 11, no. 5, pp. 288–290, 1986.

[7] A. Ashkin, "Forces of a single-beam gradient laser trap on a dielectric sphere in the ray optics regime," *Biophysical journal*, vol. 61, no. 2, pp. 569–582, 1992.

[8] R. W. Applegate, D. W. Marr, J. Squier, and S. W. Graves, "Particle size limits when using optical trapping and deflection of particles for sorting using diode laser bars," *Optics express*, vol. 17, no. 19, pp. 16 731–16 738, 2009.

[9] C. Gonzalez-Ballestero, M. Aspelmeyer, L. Novotny, R. Quidant, and O. Romero-Isart, "Levitodynamics: Levitation and control of microscopic objects in vacuum," *Science*, vol. 374, no. 6564, p. eabg3027, 2021.

[10] A. Ashkin and J. Dziedzic, "Optical levitation by radiation pressure," *Applied Physics Letters*, vol. 19, no. 8, pp. 283–285, 1971.

[11] U. Delić, D. Grass, M. Reisenbauer, T. Damm, M. Weitz, N. Kiesel, and M. Aspelmeyer, "Levitated cavity optomechanics in high vacuum," *Quantum Science and Technology*, vol. 5, no. 2, p. 025006, 2020.

[12] K. Frye, S. Abend, W. Bartosch, A. Bawamia, D. Becker, H. Blume, C. Braxmaier, S.-W. Chiow, M. A. Efremov, W. Ertmer *et al.*, "The bose-einstein condensate and cold atom laboratory," *EPJ Quantum Technology*, vol. 8, no. 1, p. 1, 2021.

[13] W. D. Phillips, "Nobel lecture: Laser cooling and trapping of neutral atoms," *Reviews of Modern Physics*, vol. 70, no. 3, p. 721, 1998.

[14] C. J. Bustamante, Y. R. Chemla, S. Liu, and M. D. Wang, "Optical tweezers in single-molecule biophysics," *Nature Reviews Methods Primers*, vol. 1, no. 1, p. 25, 2021.

[15] J. M. Goodkind, "The superconducting gravimeter," *Review of scientific instruments*, vol. 70, no. 11, pp. 4131–4152, 1999.

[16] K. Dholakia and T. Čižmár, "Shaping the future of manipulation," *Nature photonics*, vol. 5, no. 6, pp. 335–342, 2011.

[17] L. A. Defaveri, S. M. D. Queirós, and W. A. Morgado, "Dependence of efficiency on the nonlinear nature of a nanomachine," *Physical Review E*, vol. 98, no. 6, p. 062106, 2018.

[18] L. A. Defaveri, W. A. Morgado, and S. M. D. Queirós, "Power output for a nonlinear brownian machine," *Physical Review E*, vol. 96, no. 5, p. 052115, 2017.

[19] J. Gieseler and J. Millen, "Levitated nanoparticles for microscopic thermodynamics—a review," *Entropy*, vol. 20, no. 5, p. 326, 2018.

[20] J. Gieseler, R. Quidant, C. Dellago, and L. Novotny, "Dynamic relaxation of a levitated nanoparticle from a non-equilibrium steady state," *Nature nanotechnology*, vol. 9, no. 5, pp. 358–364, 2014.

[21] V. Svak, J. Flajšmanová, L. Chvátal, M. Šiler, A. Jonáš, J. Ježek, S. H. Simpson, P. Zemánek, and O. Brzobohatỳ, "Stochastic dynamics of optically bound matter levitated in vacuum," *Optica*, vol. 8, no. 2, pp. 220–229, 2021.

[22] J. Sheng, C. Yang, and H. Wu, "Nonequilibrium thermodynamics in cavity optomechanics," *Fundamental Research*, vol. 3, no. 1, pp. 75–86, 2023.

[23] Y. Arita, J. M. Richards, M. Mazilu, G. C. Spalding, S. E. Skelton Spesyvtseva, D. Craig, and K. Dholakia, "Rotational dynamics and heating of trapped nanovaterite particles," *ACS nano*, vol. 10, no. 12, pp. 11 505–11 510, 2016.

[24] R. Vogel, M. Persson, C. Feng, S. J. Parkin, T. A. Nieminen, B. Wood, N. R. Heckenberg, and H. Rubinsztein-Dunlop, "Synthesis and surface modification of birefringent vaterite microspheres," *Langmuir*, vol. 25, no. 19, pp. 11 672–11 679, 2009.

[25] A. Ashkin and J. M. Dziedzic, "Optical trapping and manipulation of viruses and bacteria," *Science*, vol. 235, no. 4795, pp. 1517–1520, 1987.

[26] T. Iakovleva, B. Sarma, and J. Twamley, "Zeptometer displacement sensing using cavity opto-magneto-mechanics," *arXiv preprint arXiv:2302.06795*, 2023.

[27] T. Westphal, H. Hepach, J. Pfaff, and M. Aspelmeyer, "Measurement of gravitational coupling between millimetre-sized masses," *Nature*, vol. 591, no. 7849, pp. 225–228, 2021.

[28] A. A. Geraci, S. B. Papp, and J. Kitching, "Short-range force detection using optically cooled levitated microspheres," *Physical review letters*, vol. 105, no. 10, p. 101101, 2010.

[29] C. Gonzalez-Ballestero, P. Maurer, D. Windey, L. Novotny, R. Reimann, and O. Romero-Isart, "Theory for cavity cooling of levitated nanoparticles via coherent scattering: Master equation approach," *Physical Review A*, vol. 100, no. 1, p. 013805, 2019.

[30] U. Delić, M. Reisenbauer, K. Dare, D. Grass, V. Vuletić, N. Kiesel, and M. Aspelmeyer, "Cooling of a levitated nanoparticle to the motional quantum ground state," *Science*, vol. 367, no. 6480, pp. 892–895, 2020.

[31] L. Magrini, P. Rosenzweig, C. Bach, A. Deutschmann-Olek, S. G. Hofer, S. Hong, N. Kiesel, A. Kugi, and M. Aspelmeyer, "Real-time optimal quantum control of mechanical motion at room temperature," *Nature*, vol. 595, no. 7867, pp. 373–377, 2021.

[32] J. Piotrowski, D. Windey, J. Vijayan, C. Gonzalez-Ballestero, A. de los Ríos Sommer, N. Meyer, R. Quidant, O. Romero-Isart, R. Reimann, and L. Novotny, "Simultaneous ground-state cooling of two mechanical modes of a levitated nanoparticle," *Nature Physics*, pp. 1–5, 2023.

[33] B. Suassuna, B. Melo, and T. Guerreiro, "Path integrals and nonlinear optical tweezers," *Phys. Rev. A*, vol. 103, p. 013110, Jan 2021. [Online]. Available: https://link.aps.org/doi/10.1103/PhysRevA.103.013110

[34] O. Kremer, D. Tandeitnik, R. Mufato, I. Califrer, B. Calderoni, F. Calliari, B. Melo, G. Temporão, and T. Guerreiro, "Perturbative nonlinear feedback forces for optical levitation experiments," 2023.

[35] L. Rondin, J. Gieseler, F. Ricci, R. Quidant, C. Dellago, and L. Novotny, "Direct measurement of kramers turnover with a levitated nanoparticle," *Nature nanotechnology*, vol. 12, no. 12, pp. 1130–1133, 2017.

[36] F. Ricci, R. A. Rica, M. Spasenović, J. Gieseler, L. Rondin, L. Novotny, and R. Quidant, "Optically levitated nanoparticle as a model system for stochastic bistable dynamics," *Nature communications*, vol. 8, no. 1, p. 15141, 2017.

[37] F. Almeida, I. Sousa, O. Kremer, B. P. da Silva, D. Tasca, A. Khoury, G. Temporão, and T. Guerreiro, "Trapping microparticles in a structured dark focus," *arXiv preprint arXiv:2302.01953*, 2023.

[38] J. Arlt and M. J. Padgett, "Generation of a beam with a dark focus surrounded by regions of higher intensity: the optical bottle beam," *Optics letters*, vol. 25, no. 4, pp. 191–193, 2000.

[39] J. Rieser, M. A. Ciampini, H. Rudolph, N. Kiesel, K. Hornberger, B. A. Stickler, M. Aspelmeyer, and U. Delić, "Tunable light-induced dipole-dipole interaction between optically levitated nanoparticles," *Science*, vol. 377, no. 6609, pp. 987–990, 2022.

[40] A. Ashkin, "Acceleration and trapping of particles by radiation pressure," *Physical review letters*, vol. 24, no. 4, p. 156, 1970.

[41] C. Rosales-Guzmán, B. Ndagano, and A. Forbes, "A review of complex vector light fields and their applications," *Journal of Optics*, vol. 20, no. 12, p. 123001, 2018.

[42] L. Novotny and B. Hecht, *Principles of nano-optics*. Cambridge university press, 2012.

[43] T. A. Nieminen, V. L. Loke, A. B. Stilgoe, G. Knöner, A. M. Brańczyk, N. R. Heckenberg, and H. Rubinsztein-Dunlop, "Optical tweezers computational toolbox," *Journal of Optics A: Pure and Applied Optics*, vol. 9, no. 8, p. S196, 2007.

[44] B. E. Saleh and M. C. Teich, *Fundamentals of photonics*. john Wiley & sons, 2019.

[45] P. H. Jones, O. M. Maragò, and G. Volpe, *Optical tweezers: Principles and applications*. Cambridge University Press, 2015.

[46] S. Albaladejo, M. I. Marqués, M. Laroche, and J. J. Sáenz, "Scattering forces from the curl of the spin angular momentum of a light field," *Physical review letters*, vol. 102, no. 11, p. 113602, 2009.

[47] M. Kardar, *Statistical physics of fields*. Cambridge University Press, 2007.

[48] T. Li, *Fundamental tests of physics with optically trapped microspheres*. Springer Science & Business Media, 2012.

[49] J. Gieseler, J. R. Gomez-Solano, A. Magazzù, I. P. Castillo, L. P. García, M. Gironella-Torrent, X. Viader-Godoy, F. Ritort, G. Pesce, A. V. Arzola *et al.*, "Optical tweezers—from calibration to applications: a tutorial," *Advances in Optics and Photonics*, vol. 13, no. 1, pp. 74–241, 2021.

[50] W. P. Bowen and G. J. Milburn, *Quantum optomechanics*. CRC press, 2015.

[51] G. B. Airy, "On the diffraction of an object-glass with circular aperture," *Transactions of the Cambridge Philosophical Society*, vol. 5, p. 283, 1835.

[52] F. Tebbenjohanns, M. Frimmer, and L. Novotny, "Optimal position detection of a dipolar scatterer in a focused field," *Physical Review A*, vol. 100, no. 4, p. 043821, 2019.

[53] F. Albarelli, A. Ferraro, M. Paternostro, and M. G. Paris, "Nonlinearity as a resource for nonclassicality in anharmonic systems," *Physical Review A*, vol. 93, no. 3, p. 032112, 2016.

[54] L. Neumeier, M. A. Ciampini, O. Romero-Isart, M. Aspelmeyer, and N. Kiesel, "Fast quantum interference of a nanoparticle via optical potential control," *arXiv preprint arXiv:2207.12539*, 2022.

[55] J. Bateman, S. Nimmrichter, K. Hornberger, and H. Ulbricht, "Near-field interferometry of a free-falling nanoparticle from a point-like source," *Nature communications*, vol. 5, no. 1, p. 4788, 2014.

[56] N. Bullier, A. Pontin, and P. Barker, "Quadratic optomechanical cooling of a cavity-levitated nanosphere," *Physical Review Research*, vol. 3, no. 3, p. L032022, 2021.

[57] T. Liang, S. Zhu, P. He, Z. Chen, Y. Wang, C. Li, Z. Fu, X. Gao, X. Chen, N. Li *et al.*, "Yoctonewton force detection based on optically levitated oscillator," *Fundamental Research*, vol. 3, no. 1, pp. 57–62, 2023.

[58] L. Paterson, M. P. MacDonald, J. Arlt, W. Sibbett, P. E. Bryant, and K. Dholakia, "Controlled rotation of optically trapped microscopic particles," *Science*, vol. 292, no. 5518, pp. 912–914, 2001.

[59] B. R. Boruah, "Dynamic manipulation of a laser beam using a liquid crystal spatial light modulator," *American Journal of Physics*, vol. 77, no. 4, pp. 331–336, 2009.

[60] B. Melo, I. Brandão, R. Rodrigues, A. Khoury, T. Guerreiro *et al.*, "Optical trapping in a dark focus," *Physical Review Applied*, vol. 14, no. 3, p. 034069, 2020.

[61] K. Dholakia and P. Zemánek, "Colloquium: Gripped by light: Optical binding," *Rev. Mod. Phys.*, vol. 82, pp. 1767–1791, Jun 2010. [Online]. Available: https://link.aps.org/doi/10.1103/RevModPhys.82.1767

[62] U. c. v. Delić, M. Reisenbauer, D. Grass, N. Kiesel, V. Vuletić, and M. Aspelmeyer, "Cavity cooling of a levitated nanosphere by coherent scattering," *Phys. Rev. Lett.*, vol. 122, p. 123602, Mar 2019. [Online]. Available: https://link.aps.org/doi/10.1103/PhysRevLett.122.123602

[63] J. A. Zielińska, F. van der Laan, A. Norrman, R. Reimann, L. Novotny, and M. Frimmer, "Full control of the libration potential in rotational levitodynamics," *arXiv preprint arXiv:2301.04536*, 2023.